New insights on the interannual surface mass balance variability on the South Shetland Islands glaciers, northerly Antarctic Peninsula

Torres, Christian; Bozkurt, Deniz; Carrasco-Escaff, Tomás; Bolibar, Jordi; Arigony-Neto, Jorge

DOI
10.1016/j.gloplacha.2024.104506

Publication date
2024

Document Version
Final published version

Published in
Global and Planetary Change

Citation (APA)
Torres, C., Bozkurt, D., Carrasco-Escaff, T., Bolibar, J., & Arigony-Neto, J. (2024). New insights on the interannual surface mass balance variability on the South Shetland Islands glaciers, northerly Antarctic Peninsula. *Global and Planetary Change*, *239*, Article 104506. https://doi.org/10.1016/j.gloplacha.2024.104506

Global and Planetary Change 239 (2024) 104506

Contents lists available at ScienceDirect

Global and Planetary Change

journal homepage: www.elsevier.com/locate/gloplacha

New insights on the interannual surface mass balance variability on the South Shetland Islands glaciers, northerly Antarctic Peninsula

Christian Torres [a,b,*], Deniz Bozkurt [b,c,d], Tomás Carrasco-Escaff [c], Jordi Bolibar [e], Jorge Arigony-Neto [a]

[a] *Institute of Oceanography, Federal University of Rio Grande, Brazil*
[b] *Department of Meteorology, University of Valparaíso, Chile*
[c] *Center for Climate and Resilience Research (CR)^2, Chile*
[d] *Center for Oceanographic Research COPAS COASTAL, Universidad de Concepción, Chile*
[e] *Department of Civil Engineering and Geosciences, Delft University of Technology, Netherlands*

ARTICLE INFO

Editor: Dr. Jed O Kaplan

Keywords:
Climate forcings
Atmospheric rivers
Surface mass balance
South Shetland Islands
Glaciers

ABSTRACT

Few studies have assessed a comprehensive understanding of how the seasonal and interannual variability and trends of the surface mass balance (SMB), including the influence of atmospheric river (ARs), are governed by the climate on the South Shetland Islands (SSI) glaciers located in the northerly Antarctic Peninsula (AP). To address this gap, we comprehensively analyzed the correlations and regressions between seasonal and annual SMB with regional to global climate indices and a state-of-the-art AR tracking database from 1980 to 2019. The daily and monthly SMB was obtained from two physical glaciological models, which was verified against 19 years of annual and seasonal glacier-wide SMB observations available in three glaciers (Johnsons, Hurd, and Bellingshausen), showing a good ability to capture interannual and seasonal variability. Results indicate a low dependence of the SMB on main atmospheric modes of variability (e.g., El Niño-Southern Oscillation and the Southern Annular Mode), and a moderate dependence on regional climate indices based on atmospheric pressure anomalies and sea surface temperature anomalies over the Drake Passage. Furthermore, our findings reveal that ARs have different effects on the SMB depending on the season. For example, winter ARs tend to boost accumulation due to increased snowfall, while summer ARs tend to intensify surface melting due to increased sensible heat flux. Our study highlights the Drake Passage as a key region that has the potential to influence the interannual and seasonal variability of the SMB and other climate variables, such as air temperature and snowfall over the SSI. We suggest that future work should consider this region to better understand the past, present and future climate changes on the SSI and surrounding areas.

1. Introduction

The Antarctic Peninsula (AP) region has become a focal point in climate science due to its rapid and pronounced response to global climate change. Since the 1950s, the AP has experienced one of the most significant warming trends on Earth (Bromwich et al., 2013). This region, home to vital ice shelves like Larsen C, is a unique and critical indicator of the ongoing environmental changes occurring on a global scale.

In the last few decades, the AP's climate has demonstrated remarkable variability at decadal time scales, with warming trends intermingling with cooling periods, offering a dynamic canvas upon which the impacts of climate change unfold. For instance, the AP region presented warming (+0.32 °C/decade during 1979–1997) and cooling (−0.47 °C/decade during 1999–2014) trends (Turner et al., 2016, 2020; Oliva et al., 2017; Carrasco et al., 2021). Furthermore, this region experienced two positive (1970–1991 = +60 mm/decade and 2000–2019 = +31 mm/decade) and one negative (1991–1999 = −95 mm/decade) annual precipitation trends (Carrasco and Cordero, 2020). These patterns have been assessed and attributed to a range of factors, from large-scale atmospheric circulation patterns to regional climate drivers, such as the Southern Annular Mode (SAM), El Niño-Southern Oscillation (ENSO), deep convection in the central tropical Pacific (DC-CPAC), and synoptic low-pressure systems (e.g., Turner et al., 2005; Marshall, 2007; Ding

---

* Corresponding author at: Institute of Oceanography, Federal University of Rio Grande, Brazil.
E-mail address: christian010194@gmail.com (C. Torres).

https://doi.org/10.1016/j.gloplacha.2024.104506
Received 11 January 2024; Received in revised form 5 May 2024; Accepted 26 June 2024

et al., 2011; Fogt et al., 2011; Fogt and Marshall, 2020; Turner et al., 2016, 2020; Gonzalez et al., 2018; Bello et al., 2022; Clem et al., 2022).

The AP's climate variability and the associated cryospheric responses are not only of scientific interest but also have profound implications for the local and global environment. Understanding the interplay between these atmospheric and cryospheric dynamics is crucial, especially as the AP is projected to experience continued warming and increased precipitation throughout the 21st century (Bozkurt et al., 2021; Vignon et al., 2021). One remarkable aspect of this evolving climate narrative is the role of extreme weather events, specifically atmospheric rivers (ARs), which have recently gained prominence in our understanding of the region's environmental dynamics (e.g., Wille et al., 2019, 2022). These concentrated moisture-laden airstreams can significantly influence temperature, precipitation, and the cryosphere in the AP.

Different glaciological models, ranging from empirical to physical, have been utilized to estimate the surface mass balance (SMB), surface melting and runoff in the AP, examining their relationship with the climate. The positive day degree (PDD) model, for example, has been successfully applied to the AP (e.g., Vaughan, 2006; Costi et al., 2018). Conversely, more complex physical models coupling atmospheric and snow-ice models have been employed to represent energy exchange processes between the atmosphere and surface in this region (e.g., Van Wessem et al., 2016; Van Wessem et al., 2018; Wille et al., 2022; Clem et al., 2022). For instance, the Regional Atmospheric Climate Model (RACMO) (Van Meijgaard et al., 2008) and Modèle Atmosphérique Régional (MAR) (Gallée and Schayes, 1994) are each coupled with a snow-ice model. RACMO and MAR, depending on their configuration, simulate the evolution of the snowpack through subroutines of snow metamorphism, surface albedo, meltwater runoff, percolation, retention, refreezing, and drifting-snow. These models rely on the surface energy balance (SEB) to determine the energy available for melting. Currently, both RACMO and MAR models generate atmospheric and glaciological data at high spatio-temporal resolution for the entire AP, 5.5 and 7.5 km horizontal resolution, respectively. In addition, some studies have used the atmospheric Polar Weather Research and Forecasting (PWRF) (Hines and Bromwich, 2008) model to estimate summer surface melt over the Larsen C ice shelf, located on the eastern AP (e.g., Clem et al., 2022; Zou et al., 2022). In general, RACMO, MAR and PWRF adequately capture the spatial and temporal variability of the AP SMB, as evidenced by comparisons with in-situ and remote sensing observations. Van Wessem et al. (2016) evaluated the RACMO-simulated AP SMB by comparing it with 132 in-situ SMB observations and data from six glacier discharge basins, showing reasonable agreement.

Previous research suggests that recent interdecadal to decadal changes in Antarctic ice mass, as determined by remote sensing or glaciological models, are influenced by both SAM and ENSO (King et al., 2023). The impacts of SAM and ENSO on the ice mass balance across the Antarctic continent exhibit notable variability. For example, during the positive phase of the SAM, negative mass anomalies are observed along much of the West Antarctic coast and southern AP, while notable positive mass anomalies are found over the northern AP (King et al., 2023). Similarly, the positive phase of ENSO tends to drive positive mass anomalies over the majority of western AP (King et al., 2023), while potentially inducing negative mass anomalies over the eastern AP (Zhang et al., 2021). However, more localized studies suggest that SAM and ENSO exert minimal influence on the mass balance and surface melting on interannual scales over West Antarctica and the AP. Clem et al. (2022) found that summer surface melting on the Larsen C Ice Shelf, located in the eastern AP, is primarily triggered by the DC-CPAC, which does not necessarily correlate with ENSO. Similarly, Donat-Magnin et al. (2020) observed that the interannual variability of summer SMB and surface melting over the drainage basins of the Amundsen Sea glaciers, in West Antarctica, is influenced by the position and intensity of the Amundsen Sea Low (ASL). Both studies suggest that ENSO or SAM have minimal or insignificant control over summer mass and melting changes in these regions.

The glacier-climate interaction on AP is complex because other climate forcing factors may have a more pronounced control on glacier mass changes. Wallis et al. (2023) demonstrated that glaciers in the western AP respond to seasonal ice-ocean-atmosphere forcing, highlighting their sensitivity to changes in glacier terminus position and surface melt, rainwater flux, and ocean temperature. Furthermore, ARs over the AP lead to extremely high-temperature events (Bozkurt et al., 2020), significant changes in precipitation patterns (Wille et al., 2021), which in turn, impact on sea ice disintegration, surface melting, and instability of ice shelves in this region (Wille et al., 2022). ARs may also have a spatially varied impact on the mass balance of glaciers and ice shelves located in AP, with positive SMB in the western AP and negative SMB in the eastern AP (Wille et al., 2022). Recently, Zou et al. (2022) reported surface melting on the entire northern AP during the formation of low-pressure and high-pressure systems, resulting in prolonged AR events.

The mass balance changes among glaciers in the northern AP can be quite varied. According to estimates by Seehaus et al. (2023), the Starbuck Glacier showed a slightly positive specific mass balance of 0.03 kg/m^2 year, while the Drygalski Glacier showed an extremely negative specific mass balance of -2.07 kg/m^2 year, both over the period 2013–2017. These changes in mass balance are mainly caused by changes in glacier-to-glacier ice dynamics. However, in much of the northern AP, the observed mass changes can be attributed to climatic mass balance variations.

As the impact of ENSO, SAM, DC-CPAC, ARs, ASL and other climate forcing on the ice mass changes vary spatially over the AP and West Antarctic, more detailed studies need to be developed to understand how these climate forcing factors impact locally in each region. Here, we focused on understanding the influence of climatic forcing factors (i.e., ENSO, SAM, DC-CPAC, ARs, ASL and others climate forcings), on the interannual and seasonal SMB of the South Shetland Islands (SSI) glaciers, situated in northern AP. These islands experience the intricate interplay of atmospheric forces, oceanic dynamics, and the ever-changing cryosphere. The surrounding oceanic forces, including sea ice extent-concentration (SIE-SIC), sea surface temperature (SST), and regional ocean circulation patterns, are integral components of the complex SSI climate system (e.g., Cook et al., 2016; Kerr et al., 2018). Recent studies have further demonstrated that the climatic conditions on the SSI are significantly shaped by specific atmospheric circulation systems, such as low-pressure systems over the Drake Passage and the Amundsen-Bellingshausen Sea (i.e., ASL) (Gonzalez et al., 2018; Torres et al., 2023).

Motivated by Carrasco-Escaff et al. (2023), whose research delved into the impact of climate on the Patagonian Icefields, our study embarks investigating the glacier-climate relationship within the SSI. Carrasco-Escaff et al. (2023) underscored the significance of a low-pressure system situated over the Drake Passage (Drake low) as a prominent driver of the positive SMB over the Patagonian Icefields, surpassing even the primary modes of climate variability, such as ENSO and SAM. In this context, our hypothesis posits that the same low-pressure atmospheric circulation system plays a pivotal role in influencing the variability of SMB among the SSI glaciers, particularly during the winter season.

The Drake low has been identified as one of five atmospheric circulation patterns over the AP (Gonzalez et al., 2018). This system significantly controls precipitation and moisture anomalies over northern AP, including the SSI (Gonzalez et al., 2018; Torres et al., 2023). Gonzalez et al. (2018) underscores that the Drake low and flow over the Drake Passage determine the largest anomalies of precipitation observed at the Spanish Base Juan Carlos I Automatic Weather Station situated on Livingston Island. Here, we define the Drake low as a typical synoptic-scale condition associated with passing frontal cyclones in the Drake Passage.

Furthermore, a comprehensive understanding of how the seasonal and interannual variability and trends of SMB, including the influence of ARs, are governed by the climate in this region is lacking. To address these knowledge gaps, our study is primarily focused on three key objectives to (1) the compare the annual and seasonal SMB obtained with three glaciological models such as PDD model, an intermediate COupled Snowpack and Ice surface energy and mass balance model in PYthon (COSIPY), and RACMO model for the period 1980 to 2019; (2) the assessment of the atmospheric and oceanic influences on SMB across seasonal and interannual timescales; and (3) the evaluation of the impact of ARs on the SMB of these peripheral glaciers.

2. Study site and data

2.1. South Shetlands Islands glaciers and their climate variability

The SSI, located in the northern AP, form one of the largest groups of islands around this region. The SSI comprises several islands, such as King George, Livingston, etc. These islands are separated by the Bransfield Strait and the Drake Passage (Fig. 1). According to Silva et al. (2020), the SSI contains 143 glaciers, among land-terminating and tidewater glaciers (70% of the total).

The climate over the northern AP, where the SSI are located, is extremely complex and varies due to several factors: (1) its northerly position, which leads to both warm-wet and cold-dry through the advection of moist and dry air from the Bellingshausen Sea and Weddell Sea, respectively; (2) its less pronounced topography, which may condition the impact of westerly winds and ARs, in contrast to the central-southern AP that has a more pronounced topographic barrier affecting temperature-precipitation-wind relationships (e.g., Clem and Fogt, 2013; Clem et al., 2016); and (3) its proximity to the Drake Passage, making it susceptible to mesoscale cyclonic systems originating from the Bellingshausen Sea, traveling west to east and reaching the Weddell Sea. Additionally, this region has been one of the fastest-warming regions on Earth since the 1950s and serves as a dynamic transitional zone between subpolar-polar and oceanic-coastal environments (Kerr et al., 2018).

Based on the observational data available from the Russian Bellingshausen station covering the period 1969 to 2020, the annual mean temperature is −1.98 ± 0.83 °C, and the annual precipitation accumulation is 967 ± 115 mm/year. Interannual temperature variability across the SSI is predominantly governed by the positioning and intensity of the ASL (Bello et al., 2022; Torres et al., 2023), but it is also moderately influenced by large-scale climate indices such as SAM and ENSO, with ENSO being more visible during spring (September to November) (Clem and Fogt, 2013; Clem et al., 2016). Conversely, the interannual variability of precipitation and snowfall over those islands is strongly influenced by mesoscale low-pressure systems originating from the Bellingshausen Sea and traversing the Drake Passage (Gonzalez et al., 2018; Torres et al., 2023), with weaker influences from ENSO and SAM (Carrasco et al., 2021). For instance, Gonzalez et al. (2018)

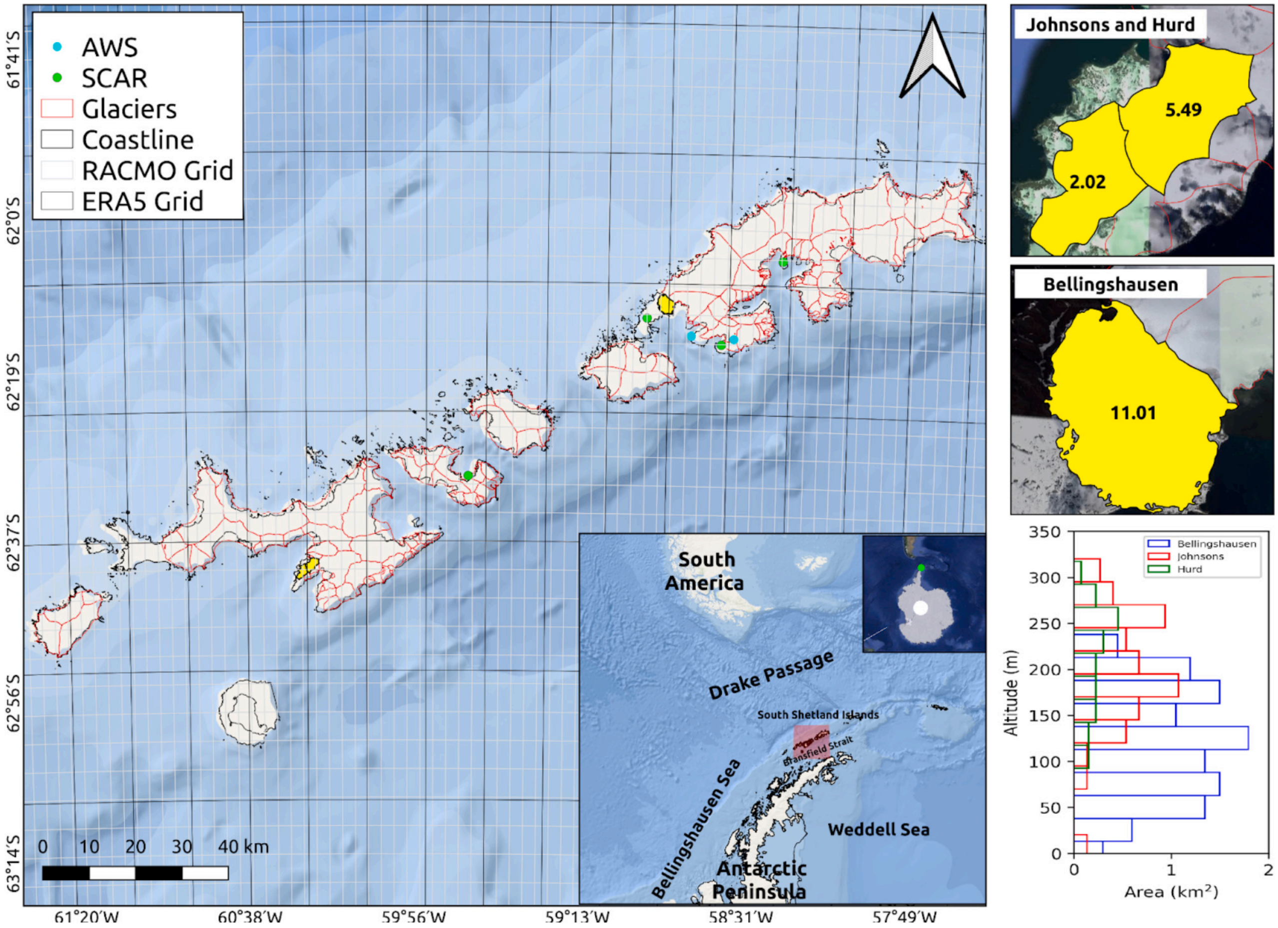

Fig. 1. Location map of the South Shetland Islands (SSI), northern Antarctic Peninsula (AP). The green dots indicate the locations of the climate stations from READER-SCAR. The cyan dots indicate the positions of the two automatic weather stations (AWS). The red outlines represent the glacier contours obtained from the Randolph Glacier Inventory, (RGI Consortium, 2017). The yellow backgrounds mark the locations of the Johnsons, Hurd and Bellingshausen glaciers. Furthermore, the Johnsons, Hurd and Bellingshausen glaciers, with their shapes and areas, are shown zoomed in the right-hand panel. Area-altitude distribution of the three glaciers are shown on the right-bottom panel with 10 altitude intervals spaced at 50 m, ranging from 0 to 350 m in elevation. The silver grids indicate the spatial resolution of RACMO (approximately 5.5 km horizontal resolution) and the black grids represent the horizontal resolution of ERA5 (approximately 31 km). (For interpretation of the references to colour in this figure legend, the reader is referred to the web version of this article.)

underscored that lows over the Drake Passage are responsible for the largest anomalies of precipitation observed at the Spanish Base Juan Carlos I on Livingston Island.

During the last decades, most glaciers on the SSI experienced shrinkage (21–70% during 1956–2018), thinning (−0.5 ± 0.6 m/year during 2012–2016), and increased surface melt (Simões et al., 2004; Rückamp et al., 2011; Pudełko et al., 2018; da Rosa et al., 2020; Pasik et al., 2021; Shahateet et al., 2021), all of which have been associated with regional warming. However, during the 2002–2011 period, these glaciers showed a decelerated rate of mass loss, attributed to increased precipitation and lower summer surface temperatures (Navarro et al., 2013; Oliva et al., 2017).

Several glaciological studies on SSI glaciers have employed remote sensing (e.g., Simões et al., 2004; Rückamp et al., 2010, 2011; Osmanoğlu et al., 2013; Pętlicki et al., 2017; Pudełko et al., 2018; Shahateet et al., 2021), in-situ observations (e.g., Molina et al., 2007; Navarro et al., 2013; Sobota et al., 2015), and modeling techniques (e.g., Bintanja, 1995; Knap et al., 1996; Braun et al., 2001; Braun and Hock, 2004; Jonsell et al., 2012; Falk et al., 2018). For instance, Braun et al. (2001) evaluated the influence of large-scale atmospheric circulation on the King George Island ice cap, located on the eastern part of the SSI, for a few case days during the summer of 1997–1998. Their results indicated maximum surface melt rates up to 20 mm w.e. per day under specific atmospheric conditions. Furthermore, Navarro et al. (2013) analyzed a decade's worth of SMB data from two glaciers, Hurd and Johnsons, on Livingston Island in the eastern SSI, revealing a notable deceleration in mass losses from 1957 to 2000 to 2002–2011. Shahateet et al. (2021) estimated the geodetic mass balance for all SSI glaciers from 2013 to 2017, providing insights into the local glacier health. Their analysis indicated a slightly negative average specific mass balance, close to equilibrium, for the entire area, with a value of −106 ± 70 mm w.e./year.

2.2. Climatological in-situ observations

We used various datasets with different periods and temporal resolutions. The first dataset was collected with an automatic weather station (AWS) installed at Fourcade and Polar Club Glacier (AWS-FPG) and represented the highest station at 194.5 m a.s.l in the SSI (Falk et al., 2018). Various hourly atmospheric variables are available in the AWS-FPG, such as incoming shortwave radiation (QSWin), incoming longwave radiation (QLWin), air temperature at 2 m (T2), relative humidity at 2 m (RH2), wind speed at 2 m (WS), surface pressure (PSFC) and total precipitation (TP) from November 2010 to May 2016. The second dataset was also collected with an AWS installed at the Korean King Sejong Station (AWS-KKS). This station also provides various atmospheric variables available daily, such as QSWin, T2, HR2, WS, PSFC and TP from January 1996 to December 2020. Finally, the third dataset includes only the T2 variable obtained at four climatological stations (Bellingshausen, Ferraz, Carlini and Arturo Prat stations) located over the SSI and made available online by the READER-SCAR (https://legacy.bas.ac.uk/met/READER/surface/stationpt.html). Fig. 1 shows the locations of the stations, and Table S1 presented their names, locations, altitudes, and periods of available data.

2.3. Glaciological in-situ observations

Very few long-term glacier monitoring programs are available on the SSI (Navarro et al., 2023). There is only one long-term program over this region, collecting data on two glaciers: Johnsons and Hurd, from 2002 to the present. Glacier-wide SMB data are freely available through the World Glacier Monitoring Service (WGMS) on seasonal and annual time scales. Additionally, other short-term (i.e., <5 years of monitoring) programs are available, such as for Bellingshausen Glacier from 2007 to 2012. We used these annual and seasonal SMB data for the Johnsons, Hurd and Bellingshausen glaciers (Fig. 1) to calibrate and validate two glaciological models to reconstruct the SMB of these glaciers from 1979 to 2019.

2.4. ERA5 reanalysis

We also used atmospheric and oceanic data from the ERA5 reanalysis produced by the European Centre for Medium-range Weather Forecasts (ECMWF) (Hersbach et al., 2020). ERA5 is provided on a regular latitude-longitude grid of approximately 31 km at hourly and monthly resolutions from 1940 to the present. Both ERA5 hourly and monthly products are available at the Copernicus Climate Data Store (https://cds.climate.copernicus.eu). We used hourly QSWin, QLWin, T2, PSFC, RH2, WS, total precipitation and snowfall from 1979 to 2019 to force glaciological models. Furthermore, we used monthly mean sea level pressure (MSLP), zonal (U) and meridional (V) wind, and geopotential height (Z) at different pressure levels, outgoing longwave radiation (OLR), SIC and SST to represent present atmospheric and oceanic conditions from 1979 to 2019.

3. Methods

3.1. Glaciological models

3.1.1. PDD model

PDD is a simple model based on the empirical relationship between temperature and surface melting of snow/ice (Braithwaite, 1995). This model has been widely used to estimate the glaciers surface melt and runoff, ice fields and ice shelves on the AP (e.g., Vaughan, 2006; Costi et al., 2018). In this study, the SMB using PDD is derived considering accumulation and surface melting processes, as described in Eq. (1).

$$SMB = ACCUM + DDice \times PDD + DDsnow \times PDD \tag{1}$$

Accumulation ($ACCUM$) is summed directly as solid precipitation (i.e., snowfall). The melt component ($DDice \times PDD + DDsnow \times PDD$) is calculated by multiplying the sums of positive temperatures over a specific period (here $n = 8$ h) by snow ($DDsnow$) and ice ($DDice$) melting factors. Here, the temperature threshold above which melt occurs is 0 °C (Costi et al., 2018). We used the same routine with the PDD model that was made available by Temme et al. (2023). This routine was used by these authors to model the mass balance at the Monte Sarmiento Massif, Tierra del Fuego.

3.1.2. COSIPY model

COSIPY is a multi-layer physical model based on the SEB (Sauter et al., 2020) approach. The SEB model combines all energy fluxes impacting the glacier surface energy budget, i.e., SWin, surface albedo (ALBEDO), LWin and outgoing longwave radiation (QLWout), turbulent sensible (QH) and latent (QLE) heat fluxes, ground heat flux (QG), and rain heat flux (QRain). QSWin and QLWin can be provided in the input data, whereas QLWout, QH, QLE, QG and QRain are derived by solving the heat equation (Sauter et al., 2020). This model is widely used in several glaciological studies worldwide due to its user-friendly implementation and free access. COSIPY considers various accumulation and ablation processes to estimate the SMB at high temporal resolution (hourly), following Eq. (2).

$$SMB = ACCUM + MELT + SUB + DEP + EVA + subMELT + REFRE \tag{2}$$

We calculated the SMB, which considers accumulation ($ACCUM$), melting ($MELT$), sublimation (SUB), deposition (DEP) and evaporation (EVA), subsurface melting ($subMELT$) and refreezing ($REFRE$). These components are determined from the available energy, resulting from the SEB, which integrates solar and atmospheric radiation, albedo, turbulent heat fluxes, ground heat and heat from rainfall. In COSIPY, the discharge is assumed to be the sum of the total water percolating through the snow/ice cover due to melting, condensation, and moisture content. More detailed information on COSIPY and its physical parameterisations can be found in Sauter et al. (2020).

3.1.3. RACMO model outputs

Additionally, we incorporated monthly QSWin, T2, snowfall and SMB data from RACMO for comparison with our simulations. RACMO is a regional high spatial resolution atmospheric and glaciological product available for the entire AP at a 5.5 km horizontal resolution from 1979 to the present (Van Wessem et al., 2016, 2018). RACMO outputs are used to force a glaciological firn densification model (FDM). The SMB in that FDM is calculated considering accumulation, melting, drifting snow and runoff processes, following Eq. (3).

$$SMB = PR - SUs - SUds - ERds - RU \tag{3}$$

where PR represents total precipitation (snowfall plus rain), SU denotes surface (SUs) plus drifting snow ($SUds$) sublimation, $ERds$ corresponds to drifting snow erosion/deposition (caused by divergence/convergence in the horizontal drifting snow flux) and RU stands for meltwater runoff, the amount of liquid water (melt and rain) that is not retained or refrozen in the snowpack. More details on the FDM can be found in Ligtenberg et al. (2011). Van Wessem et al. (2016) and Van Wessem et al. (2018) found that while RACMO realistically simulates the strong spatial precipitation variability, significant biases remain as a result of the highly complex topography of the AP.

3.2. Bias correction of ERA5

To facilitate comparisons with in-situ observations and to force our glaciological models, we carried out preprocessing steps on ERA5 data. First, we applied a bias correction to ERA5 data at the precise locations of the AWS-FPG and AWS-KKS meteorological stations. Second, we also applied a bias correction to the forcing variables at the centroid of each of the three glaciers (Johnsons, Hurd and Bellingshausen) to force the PDD and COSIPY models.

The bias correction preprocessing involved T2, dewpoint temperature (T2D), PSFC and WS. For T2 and T2D, a temperature lapse rate was used to adjust the ERA5 T2 (1 K/100 m) and T2D (0.9 K/100 m) to values corresponding to the AWS and glaciers' centroid elevations. These temperature lapse rates showed a better fit than those observed at AWS-FPG (see Figs. S1, S2 and S3). Likewise, the ERA5 PSFC was adjusted to a value corresponding to the AWS and glaciers centroid elevations, using the barometric Eq. (S1) in the supplementary material. The WS at ERA5, initially at 10 m was adjusted to 2 m using the logarithmic wind profile, Eq. (S2) in supplementary material. Finally, QSWin, QLWin, snowfall and total precipitation were obtained directly from ERA5 to compare and force glaciological models. Several studies indicated that the ERA5 dataset provides the most accurate depiction of the recent Antarctic climate (e.g., Gossart et al., 2019; Tetzner et al., 2019; Bozkurt et al., 2020; Hillebrand et al., 2021).

3.3. Glaciological modeling

Both glaciological models (PDD and COSIPY) were configured at a single point since a single ERA5 grid covers the entire glacier area. The average elevation for each glacier was obtained using the glacier outlines available from the Randolph Glacier Inventory (RGI Consortium, 2017) and a new high-resolution digital elevation model (DEM) from the gapless 100-m reference elevation model of Antarctica (Gapless-REMA100) as provided by Dong et al. (2022). To force the glaciological models, climate variables were extracted from the nearest ERA5 grid point for each glacier and averaged (QSWin, QLWin, T2, RH2, WS and PSFC) or summed (total precipitation and snowfall) over six-hour time steps. Therefore, the glaciological models were run at six-hour intervals to manage computational demands.

PDD requires only two atmospheric variables as input (temperature and precipitation or snowfall) and has very few free parameters requiring calibration. In contrast, COSIPY demands several atmospheric variables as input (QSWin, QLWin, T2, RH2, PSFC, WS and total precipitation and/or snowfall) and entails the calibration for multiple free parameters.

In both PDD and COSIPY, accumulation is directly derived from snowfall from ERA5, eliminating the need for free parameters like temperature thresholds commonly used to distinguish between solid and liquid precipitation in total precipitation. Additionally, snowfall in ERA5 is already provided in mm water equivalent (w.e.) and does not require conversion using snow/ice density, thus avoiding the use of density parameters. T2, RH2 and PSFC underwent a bias correction (see Section 3.2), adjusting for the average-elevation of each glacier. QSWin, QLWin, snowfall and total precipitation are also directly obtained from ERA5 without prior preprocessing. Several studies have employed these downscaling strategies to drive long-term glaciological models (e.g., Weidemann et al., 2018; Arndt et al., 2021; Temme et al., 2023). Finally, these three atmospheric datasets of each glacier were used in the experiment simulations.

PPD and COSIPY were optimized using a Randomized Grid Search (RGSearch) technique (e.g., Bergstra and Bengio, 2012). RGSearch, widely used in machine learning, combines Grid Search and Random Search. Instead of evaluating all possible combinations, it randomly samples a specified number of combinations from the free parameters space. Therefore, the free parameters of both PDD and COSIPY were varied randomly within their specified ranges (see Table S2) over 1000 model runs, similar to Mölg et al. (2012). The optimal combination of parameters was that with the minimum RMSE between the observed and modeled SMB during the period calibration (from 2002 to 2011). The validation of the simulations was carried out using an out-of-sample dataset from 2012 to 2019. In PDD, we focused solely on calibrating two free parameters, the DDF_{ice} and DDF_{snow} melt factors. In contrast, for COSIPY, we focused on eight key free parameters associated with the physical parameterization schemes of surface albedo and roughness.

We employed the default COSIPY configuration for the initial conditions, using three months as a spin-up period. In other words, although the simulations start on 1 January 1969, data from 1 April 1969 is used for the analysis. We have included the complete COSIPY configuration (parameterization options, initial conditions, etc.) in the Table S2 of the supplementary material.

3.4. SMB seasonal denominations, glaciological model intercomparison and statistical analysis

Throughout this study, we used the hydrological year in the Southern Hemisphere (SH), which starts on 1 April and ends on 31 March of the following year for the annual analysis. For seasonal analysis, winter was considered from 1 April to 30 November and summer was defined from 1 December to 31 March of the following year. To avoid confusion, we referred to these seasonal timescales as winter (April to November) or summer (December to March).

Given that PDD and COSIPY utilize a single point configuration, as opposed to RACMO's distributed configuration, we compared the SMB obtained with all three models. This comparison, summarized in the averaged SMB series named GLAS_PDD and GLAS_COSIPY for PDD and COSIPY, respectively, and GLAS_RACMO for RACMO, allows us to assess the impact of the model configuration on the annual and interannual SMB (Fig. S4b and c). We also obtained an averaged SMB series for all grids overlapping the SSI (Fig. S4a), called SSI_RACMO.

For the verification and validation between observations and modeling or reanalysis data, we used Pearson's or Spearman's correlation coefficient (r), bias (Bias), and root mean square error (RMSE). For the statistical analysis, Pearson's correlations and linear regression analyses were conducted, with significance testing (confidence level of 90% and 95%) based on detrended time series. Finally, the Mann-Kendall test was used to evaluate trends with a confidence level of 95%.

3.5. *Sensitivity analysis*

Extensive sensitivity analyses were performed using the COSIPY model to ensure the robustness of the interannual variability of the SMB from 1980 to 2020. In our case, COSIPY presents two primary sources of uncertainty, stemming from the model itself and from the input climate data (Arndt et al., 2021).

3.5.1. *Sensitivity to main model parameters*

We examined the influence of eight key COSIPY model parameters (related to albedo scheme and surface roughness, Table S2) on SMB. Using the RGSearch-optimized parameters as a reference. We evenly spaced each parameter within 10 steps in a given interval. Next, each element was modified while keeping other parameters constant. We compared the resulting SMB series with the optimized series to assess correlation and standard deviation.

3.5.2. *Sensitivity to the mean value of the meteorological input*

We investigated whether potential biases in the average condition of meteorological input. Introducing an offset (ΔT) to temperature and weighting snowfall with a factor (P0), we ran the SMB model for each pair of values and compared it with the optimized SMB series. We also compared the resulting SMB series with the optimized series to assess correlation and standard deviation.

3.5.3. *Sensitivity to the interannual variability of the meteorological input*

We analyzed the sensibility of the modeled SMB to interannual variability of the meteorological variables (e.g., snowfall, temperature and insolation). We removed the annual variability from one of the meteorological variables while the other two remained unchanged, similar to Carrasco-Escaff et al. (2023). To do this, we calculated the annual cycle of each variable at a time resolution of 6 h, and then used that cycle repeatedly to feed the SMB model. Rerunning COSIPY, we computed a new SMB time series and assessed dependence using squared correlation (R^2). A high R^2 suggests low dependence on year-to-year variations, while a low R^2 suggests high dependence in terms of interannual variability.

3.6. *Large-, synoptic-, and regional- scale climate indices and AR data*

The ENSO indices (such as El Niño 3, 3.4 and 4 regions) were obtained from the National Oceanic and Atmospheric Administration Climate Prediction Center (https://www.cpc.ncep.noaa.gov/) to assess potential tropical-polar teleconnections. We also constructed a customized climatic index DC-CPAC with a large-scale perspective, using a sector delineated in the central tropical Pacific (10–15°S, 170–165°W, see the pink box in Fig. 2) by Clem et al. (2022) to obtain a monthly time series of the area-averaged Outgoing Longwave Radiation (OLR). Recent studies have indicated that deep convection in the central tropical Pacific region triggers ARs making landfall at the AP (e.g., Clem et al., 2022).

The SAM and ASL are the large- and synoptic-scale atmospheric circulation which influence the climate changes in the AP. The SAM is characterized by pressure variability between the mid and high southern latitudes, influencing the strength and position of the midlatitude jet. ASL is a climatological low-pressure center located over the southern end of the Pacific Ocean, off the coast of West Antarctica. Both SAM (https://legacy.bas.ac.uk/met/gjma/sam.html; monitored using Marshall (2003) observation-based index) and ASL (https://climatedataguide.ucar.edu/climate-data/amundsen-sea-low-indices) were obtained from National Center for Atmospheric Research Climate Data Guide.

In addition to the large- and synoptic-scale indices, we constructed regional-scale climate indices over three key sectors: the Drake Passage (hereafter Drake; aqua box in Fig. 2), the Amundsen-Bellingshausen Sea (hereafter ABSea; magenta box in Fig. 2) and the Weddell Sea (hereafter WSea; blue box in Fig. 2), which directly are associated with the climate in the SSI. Monthly time series of SIE and SST are obtained from ABSea and WSea as area-averaged due to their strong relationship with temperature in SSI (Torres et al., 2023).

We identified the Drake Passage (85°W-40°W, 62.5°S-55°S, aqua box in Fig. 2) from west to east with significant correlations between SMB and Z500 during winter, annual and summer timescales, respectively. From this region, monthly time series of MSLP, Z500, T500 and SST were obtained as area-average. This sector was also contrasted with previous studies indicating the different low-pressure systems over the AP and their associated impacts on temperature and precipitation phase (rainfall and snowfall) (Gonzalez et al., 2018; Wang et al., 2021; Torres et al., 2023).

All atmospheric and oceanographic variables (i.e., ORL, MSLP, Z500, T500, SST, SIE) used to construct our large and regional indices were obtained from the monthly ERA5 reanalysis dataset. Then, the monthly anomaly of each variable is calculated independently. The last procedure is also applied for ASL since we used the area-average sea level pressure over the sector (170°E-298°E, 60°S-80°S) defined by Hosking et al. (2016).

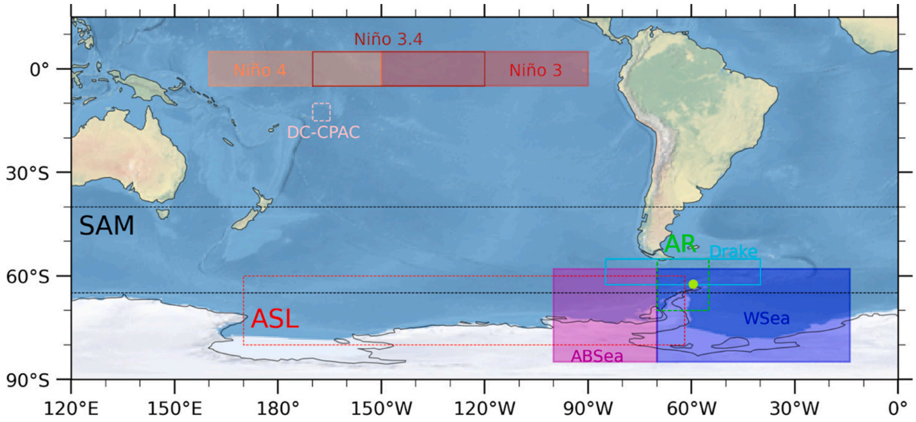

Fig. 2. Regions used for the construction of climate indices. The green dot indicates the location of the SSI. Amundsen-Bellingshausen (100–70°W; 85–55°S) and Weddell (70–14; 85–55°S) Seas regions limits were obtained from Fogt et al. (2022). Deep convection over the central tropical Pacific (170 W–165 W; 15S—10S) region limit was obtained from Clem et al. (2022). ASL limit (170°E-298°E, 60°S-80°S) was obtained from Hosking et al. (2016). Drake region (85°W-40°W; 62.5°S-55°S) was obtained from correlation analysis between winter, annual and summer SMB and Z500. The lime dashed box (70°W-55°W; 55°S-70°S) indicates the area where the ARs frequency is selected and area-averaged. (For interpretation of the references to colour in this figure legend, the reader is referred to the web version of this article.)

Finally, AR frequency was used to evaluate its impact on the glaciers over the SSI. AR frequency data were obtained from state-of-the-art AR tracking databases (1979–2018) available from Guan and Waliser (2019). Monthly time series for AR frequency were constructed for the area of 50 W–80 W and 55S—75S (green dashed box in Fig. 2). The AR frequency was calculated independently for each grid cell within the box by counting the number of 6-hourly time steps with AR conditions (i.e., grids within detected AR shape boundaries) and dividing by the total number of 6-hourly time steps during the analysis period. The AR frequency is expressed in units of days (i.e., one 6-h AR step = 0.25 days).

4. Results

4.1. SMB validation and glaciological models intercomparison

Fig. 3 shows the annual, winter (April to November), summer (December to March) time series of modeled SMB using different glaciological models (i.e., PPD, COSIPY and RACMO) from 1980 to 2019, alongside the observed SMB from 2002 to 2019, calculated as the average of the three glaciers. The same analysis also was attached for each glacier in supplementary material (Figs. S5 for annual, S6 for winter and S7 for summer). The PDD and COSIPY glaciological models were run using a set of optimal parameters (Table S2) determined through an RGSearch technique (Section 3.3, Figs. S8 and S9). The statistical indicators for calibration (2002 to 2011), validation (2012 to 2019) and comparison (2002 to 2019) periods are also included in Table S3. Additionally, Table S4 summarizes the mean, SD, minimum, and maximum of the SMB annual, winter and summer for calibration, validation and comparison periods.

For the validation period (2012–2019), our results reveal that all models have good agreement with the annual, winter and summer observed SMB: RACMO (*r* = 0.90, Bias = 8 mm w.e. and RMSE = 149 mm w.e.), PDD (*r* = 0.82, Bias = 21 mm w.e., and RMSE = 221 mm w.e.) and COSIPY (*r* = 0.83, Bias = −43 mm w.e., and RMSE = 194 mm w.e.) for annual timescale.

For the comparison period (2002–2019), the mean annual SMB-modeled was more positive by PDD (129 ± 448 mm w.e., mean ± SD), followed by RACMO (125 ± 353 mm w.e.) and by COSIPY (93 ± 275 mm w.e.). The mean SMB-modeled by COSIPY is closer to the observed SMB (40 ± 371 mm w.e.) with a slight difference (53 mm w.e.) and no significant difference in SD. In terms of magnitude, all models underestimate the SMB during the annual, winter and summer timescales.

The time series GLAS_PDD, GLAS_COSIPY, GLAS_RACMO and SSI_RACMO were also used to analyze the correlation and differences between them (see Section 3.4). We find high correlations and no statistical differences (t-student test appended) between the different annual and seasonal SMB series, even when compared to the series from SSI_RACMO (Table S5). This indicated that SMB modeling shows a similar behavior across models. Therefore, whether using a single-point or distributed model configuration does not impact the final glacier-wide SMB results for the SSI. For the analysis of climatic influences and ARs on SMB, temperature, and snowfall, we utilized the time series from SSI_RACMO, which encompasses all SSI grids. Additionally, we used COSIPY outputs for more detailed analysis of ARs impact and SMB sensitivity.

4.2. SMB interannual variability and trends

Using the SSI_RACMO time series, the mean annual SMB was positive 109 ± 321 mm w.e./year, ranging from −688 to 747 mm w.e./year over the entire period (1980–2019) (Table S6). During winter, the modeled SMB increases up to 486 ± 77 mm w.e., while during summer it decreases down to −377 ± 300 mm w.e.

The trend of the annual SMB of SSI glaciers from 1980 through 2019 showed a signal break (Fig. 4), reflecting the surface temperature trends

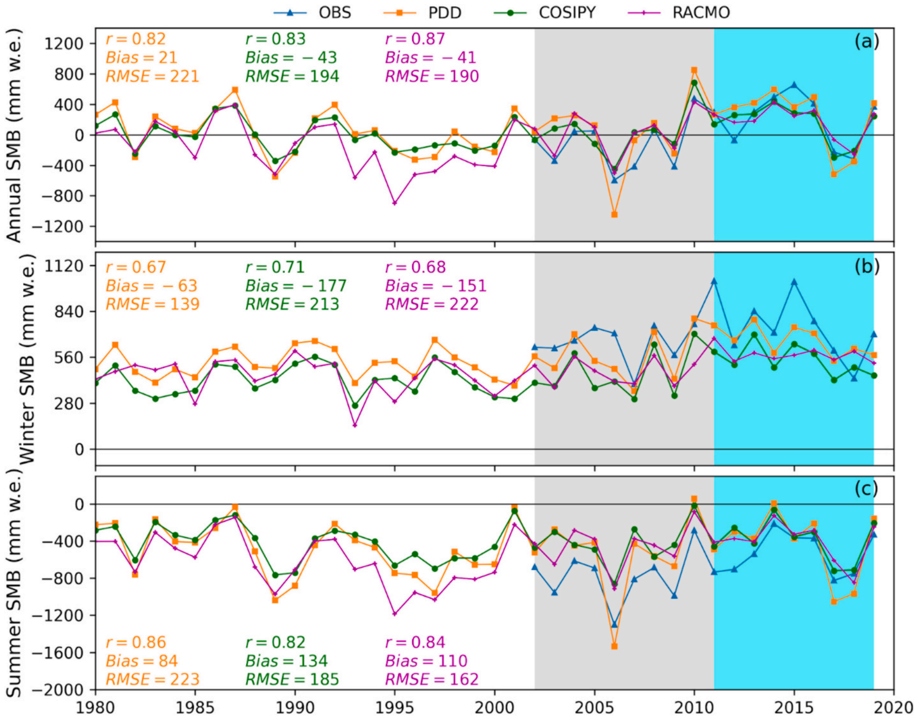

Fig. 3. Annual (a), winter (b) and summer (c) surface mass balance intercomparison between observation and reconstruction from three glaciological models (blue line OBS, and orange line PDD, green line COSIPY and magenta line RACMO models). Both PDD and COSIPY models were forced using the global reanalysis ERA5-downscaled. Gray shaded areas indicate the calibration period (2002−2011) and aqua shared areas show validation period (2012–2019). Note all statistical indicators as well correlation coefficient (r), Bias and root mean square error (RMSE) were calculated for the validation period (2012–2019). (For interpretation of the references to colour in this figure legend, the reader is referred to the web version of this article.)

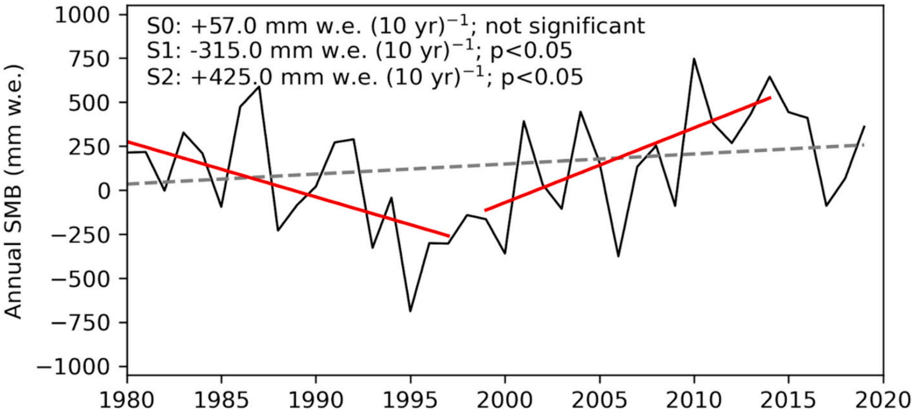

Fig. 4. Annual (April to March) surface mass balance from 1980 to 2019 based on the SSI_RACMO time series. The red lines show the linear trends for the periods 1980–1997 and 1999–2014. S0 corresponds to the entire period. S1 (1980–1997) considers the years of warming, and S2 (1999–2014) considers the years of cooling that are well-documented over the region. (For interpretation of the references to colour in this figure legend, the reader is referred to the web version of this article.)

of the AP region (compared with Fig. 4 in Carrasco et al., 2021). During 1980–1997, the trend was negative (−315 mm w.e./decade), and during 1999–2014, it was positive (+425 mm w.e./decade), with both cases being statistically significant ($p < 0.05$). The break in the trend influenced the analysis of the SMB trend for the entire period, showing a positive but statistically non-significant trend (+57 mm w.e./decade; not significant). However, a declining trend has emerged in recent years and this trend is clearly illustrated by the period from 2015 to 2019, where the SMB values once again turned negative (e.g., SMB = −89 mm w.e in 2017).

4.3. *Local-scale control over the SMB*

Fig. 5 shows the annual time series of the modeled SMB, accumulation, ablation, precipitation, temperature, and insolation, calculated as the spatial average of SSI glaciers from RACMO (SSI_RACMO time series). Winter and summer time series of the same variables also are attached on supplementary material (Figs. S10 and S11). Furthermore, correlation analysis of annual, winter and summer SMB with accumulation, ablation, snowfall, temperature and solar insolation are presented in Table S7.

The annual SMB shows a high negative correlation with ablation ($r = -0.95$, $p < 0.05$) and a moderate positive correlation with

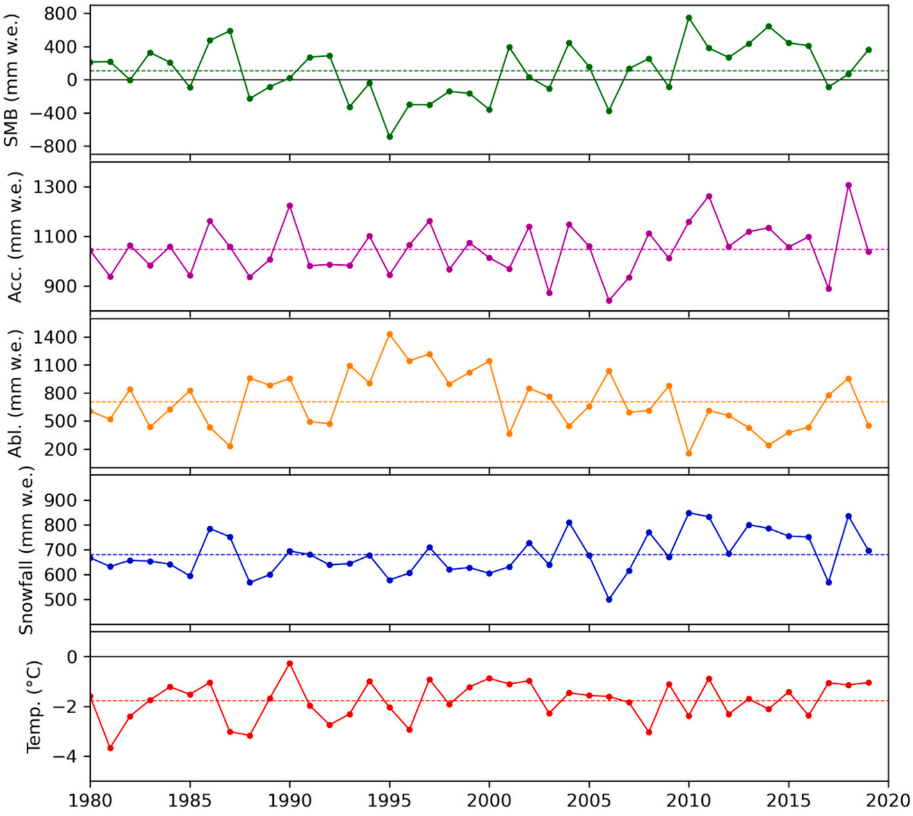

Fig. 5. Annual (April to March) time series of spatially averaged (over the area of the SSI glaciers) fields from SSI_RACMO of (from top to bottom) SMB, accumulation, accumulated snowfall, ablation, mean near-surface temperature, and mean insolation. Each segmented line indicates the mean value of the series. The gray horizontal line corresponds to the SMB zero isoline.

accumulation ($r = 0.40$, $p < 0.05$). In contrast, winter SMB shows a high positive correlation with accumulation ($r = 0.89$, $p < 0.05$) and a moderate negative correlation with ablation ($r = -0.33$, $p < 0.05$). Similar to the annual SMB, summer SMB demonstrates a high negative correlation with ablation ($r = -0.99$, $p < 0.05$) and a low correlation with accumulation ($r = 0.26$, no-significant). Additionally, from the correlation analysis between annual, winter and summer of the SMB for the period 1980–2019, we observed that the annual SMB is strongly related to the summer SMB ($r = 0.97$, $p < 0.05$) and moderately related to the winter SMB ($r = 0.46$, $p < 0.05$). These results indicate that the annual variability of the SMB is mainly controlled by ablation which is related to air temperature and moderately by accumulation which is related to snowfall.

To support the findings above, we have developed different sensitivity tests using the COSIPY model. We used these outputs to explain the impact of temperature and snowfall on the SEB and SMB components. One experiment involved adjusting the temperature by an offset and modifying the snowfall by a factor. The temperature varied by ±1 °C and the snowfall by ±20%. We used five outputs with neutral (no changes in temperature and snowfall), cold (−1 °C air temperature), warm (+1 °C air temperature), dry (−20% snowfall) and wet (+20% snowfall) conditions. The results, presented in Table S8 in the supplementary material, show that glacier SEB and SMB are highly sensitive to changes in air temperature and less so to changes in snowfall. Small changes for the SEB components such as QLWout and QH and QLE were observed when introducing a temperature offset. Conversely, large changes for the SMB components, particularly surface melting, which increased by a factor of 10.6 with the temperature adjustment, were noted.

4.4. Regional-scale control over the SMB

We conducted linear correlations and regressions analysis between the SMB from SSI_RACMO time series and different climate variables from ERA5 (i.e., precipitation, near-surface temperature, and horizontal wind at 10 m above ground level and 500 hPa) for the period 1980–2019 to assess the regional climate control on the variability of the SMB in the SSI during annual, winter, and summer timescales. Additionally, we computed latitudinal profiles of regressions of the annual, winter and summer SMB with the mean annual fields of zonal wind, geopotential height, and air temperature at a longitude of 58° W. The results are presented in Fig. 6 for annual, Fig. 7 for winter, and Fig. 8 for summer. The same analysis was performed using GLAS_COSIPY time series (Figs. S12, S13 and S14). For simplicity, we focus our analysis on the

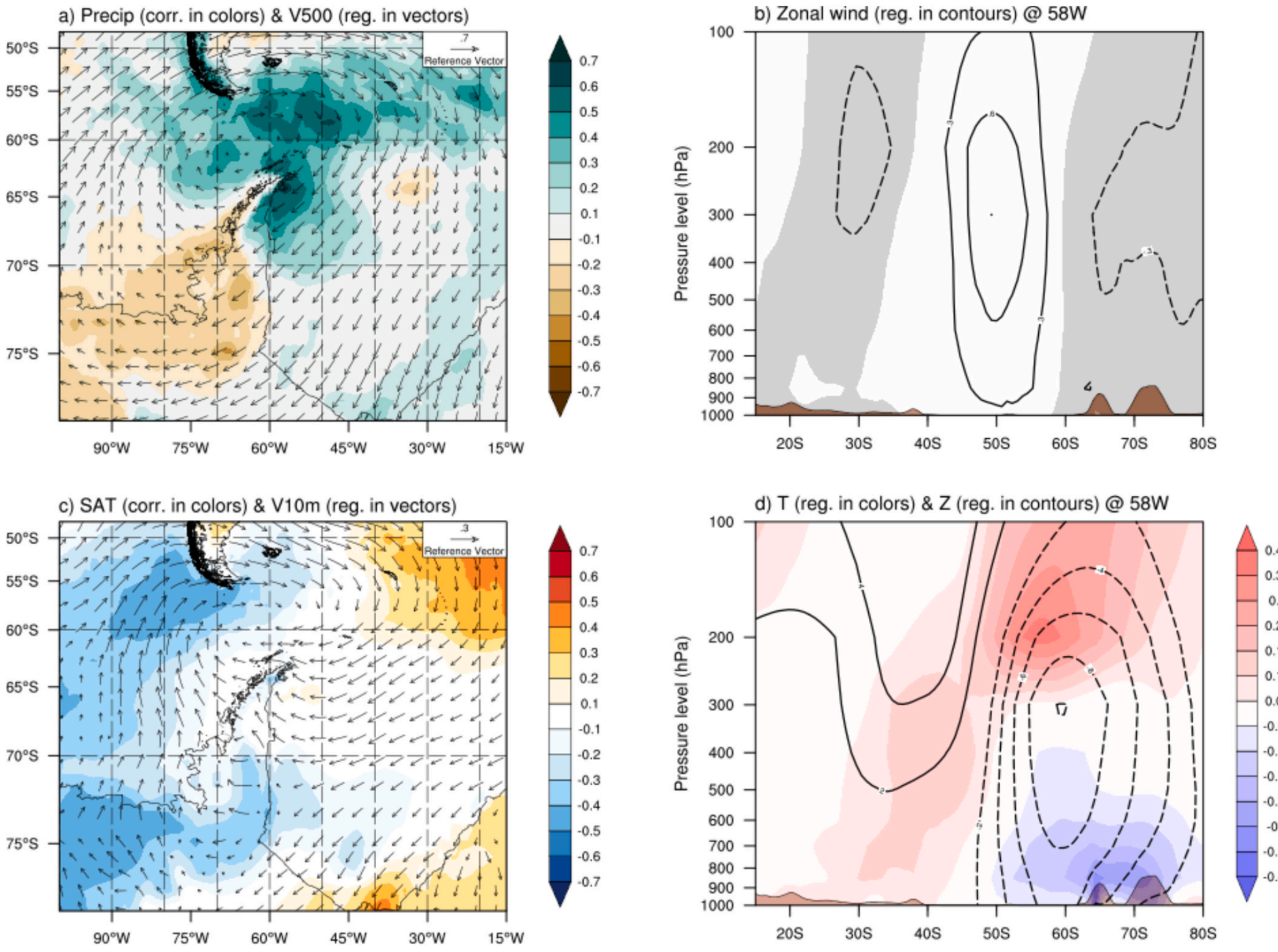

Fig. 6. Regional correlation and linear regression maps of the annual (April to March) SMB from the SSI_RACMO time series and ERA5 reanalysis. (a) Regression with annual fields of horizontal wind at 500 hPa (vectors in m/s per SD) and correlation with accumulated precipitation (colors). (b) Latitudinal and atmospheric profile of the regression with annual fields of zonal wind (contours in m/s per SD) for a transect at 58°W. Negative regression values are shaded. (c) Regression with annual fields of horizontal wind at 10 m above ground level (vectors in m/s per SD) and correlation with the mean near-surface air temperature (colors). (d) Latitudinal and atmospheric profile of the regression with annual fields of geopotential height (contours in gpm per SD, where gpm stands for geopotential meters) and temperature (colors in °C per SD) for a transect at 80° W.

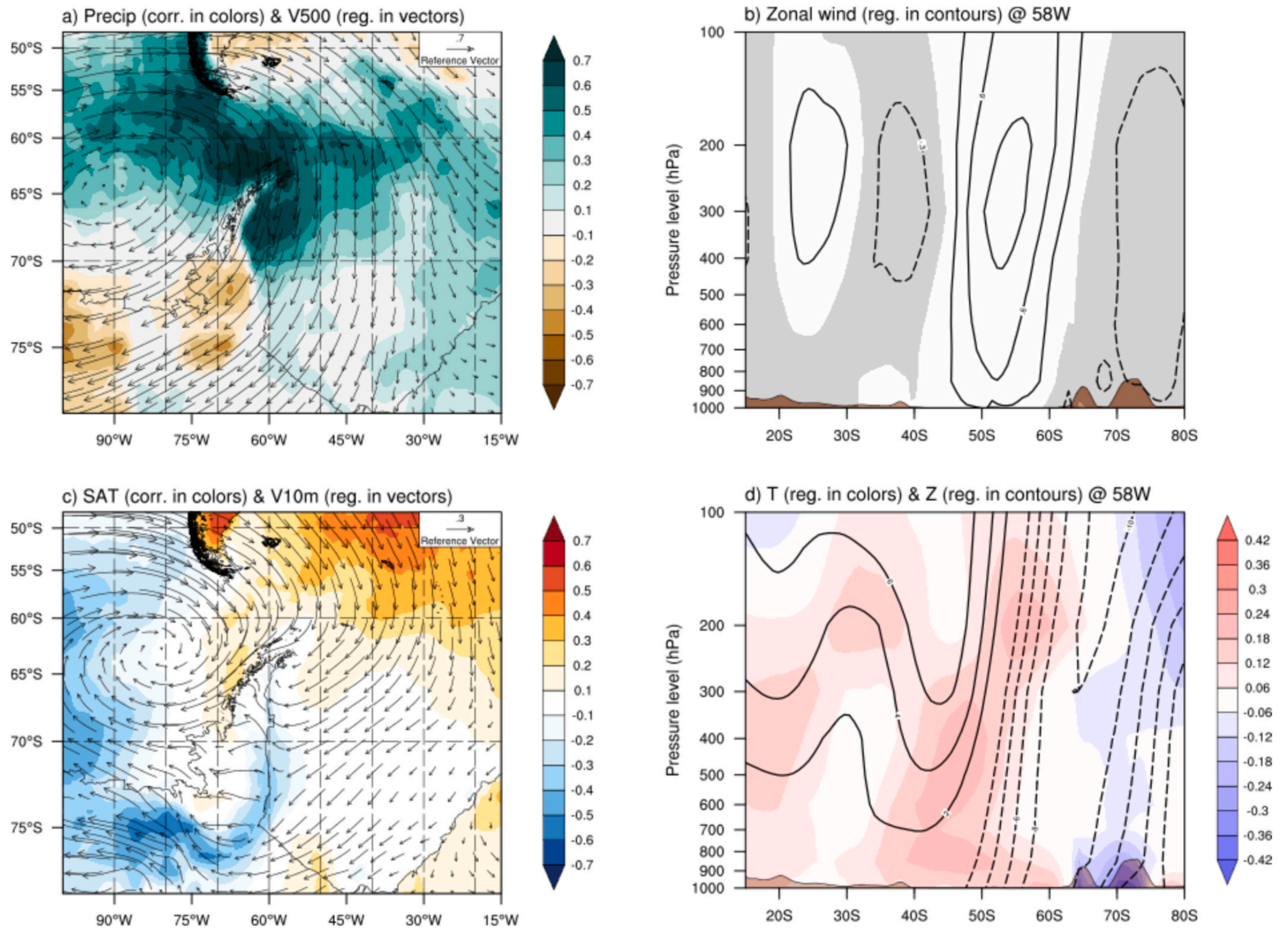

Fig. 7. The same as in Fig. 6 but for the winter (April to November).

years when the SMB is above the mean value (the analysis extends linearly to other cases).

The results show positive correlations between annual SMB and precipitation over the Drake Passage and the western part of the South Atlantic Ocean (Fig. 6a), which extends over the SSI. The regression analysis between annual SMB and the zonal wind at 500 hPa indicates the presence of a cyclonic atmospheric circulation system over the Drake Passage (Drake low), with its core located in the north-western part of the SSI (Fig. 6a). This system favors convective processes, cloud formation, and precipitation over the Drake region. The Drake low has been identified as one of five atmospheric circulation patterns over the AP that have significant impacts on precipitation and moisture variability over the SSI (Gonzalez et al., 2018; Torres et al., 2023). Furthermore, the annual SMB shows a negative correlation with the temperature over the southeastern Pacific Ocean and the AP, which also extends over the SSI (Fig. 6c). The regression analysis between SMB and the zonal wind at 10 m also shows the presence of this cyclonic system over Drake, extending over northern Bellingshausen Sea and the northern Weddell Sea. This system favors the entry of cold and dry air masses from the Weddell Sea (Fig. 6c). In addition, according to annual latitudinal profiles regressions analysis, the westerlies show negative (positive) anomalies from 80°S to near 60°S (from 58°S to near 40°S), indicating a weakening of these winds over the AP and an increase over south of South America (Fig. 6b). Negative geopotential height anomalies are observed from 80°S to 45°S, reaching their maximum around 60°S, at all levels of the atmosphere (Fig. 6b).

Analyzing the seasonal differences, during winter, years with positive SMB are characterized by the stronger presence of a cyclonic circulation and a more pronounced increase in precipitation over the Drake region (Fig. 7a). Additionally, during summer, a cyclonic circulation system over the northern Weddell Sea favors a cooling regional effect on the northern AP and Bellingshausen-Drake Seas, caused by the entry of cold air from the southern Weddell Sea and AP (Fig. 8c).

4.5. Large-scale control over the SMB

In addition, we conducted linear correlations and regression analyses between the SMB from SSI_RACMO and different climatic variables from ERA5 (i.e., MSLP, near-surface temperature (SST in ocean area plus T2 in continental area), U500 and V500 wind components, geopotential height at 300 hPa, and OLR) for the period 1980–2019 to assess the large-scale climate control on the variability of SMB in the SSI during annual, winter, and summer timescales. The results are shown in Figs. 9, 10 and 11. The same analysis also was performed using GLAS_COSIPY time series (Figs. S15, S16 and S17). As in the regional analysis, in this section, we also focus on the years with positive SMB.

Highly negative correlations are observed between the annual SMB and SST over the Drake Passage (Fig. 9a). The Drake Passage also is characterized by the presence of a low-pressure system, based on MLSP, extending longitudinally from the northern Bellingshausen Sea to the northern Weddell Sea (95°W-25°W) and latitudinally from southern AP to southern South America (75°S-45°S) (Fig. 9a). In addition, the regression analysis between SMB and the zonal wind at 500 hPa (V500) shows a cyclonic circulation system with a center located over the Drake

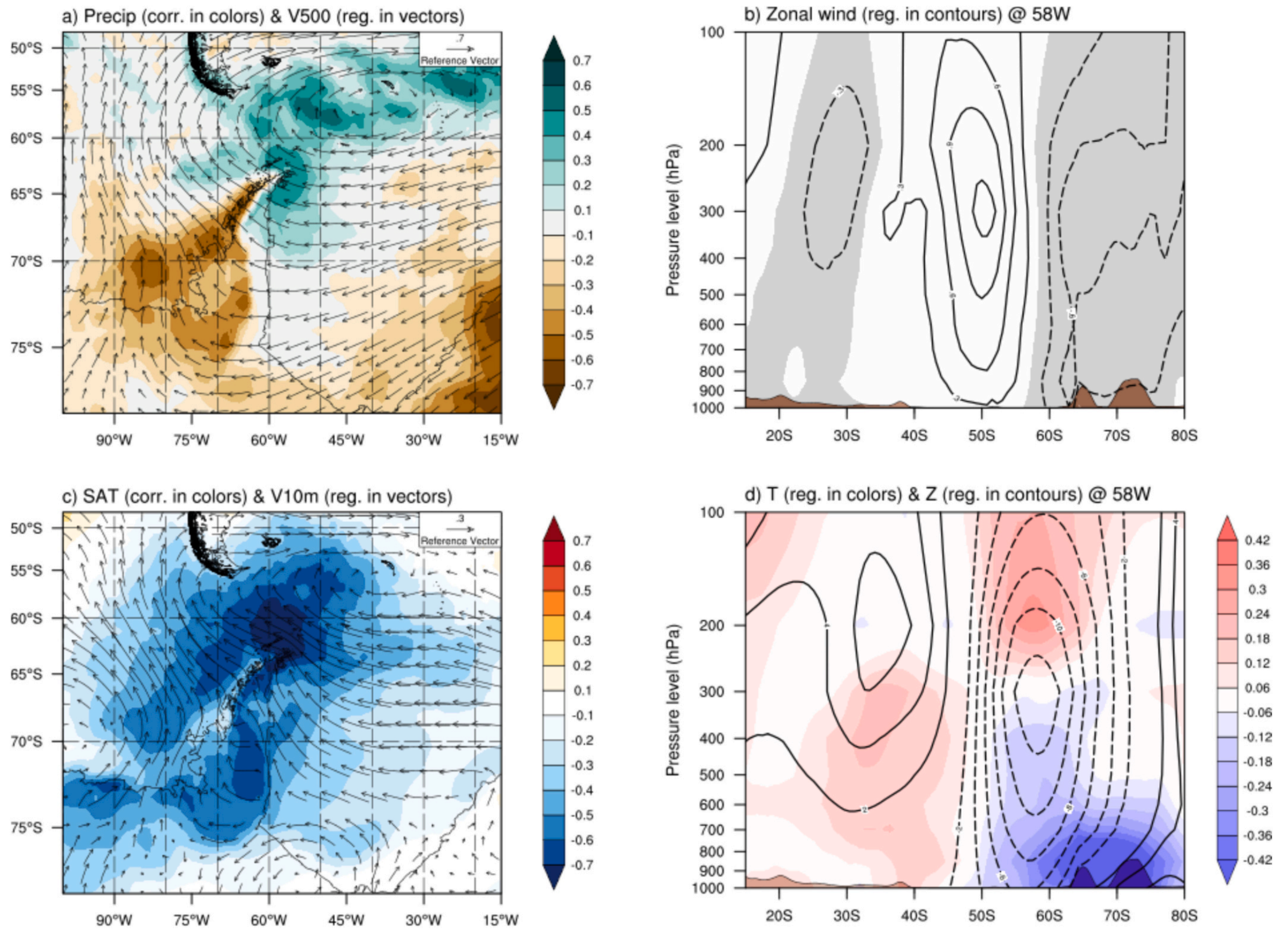

Fig. 8. The same as in Fig. 6 but for the summer (December to March).

Passage (Fig. 10b), extending over the same region as the low-pressure system. Thus, anomalies of the SST, and surface and atmospheric pressure over the Drake and surrounding regions can play an important role in the SSI SMB.

Conversely, a weak, non-significant positive correlation is shown between the annual SMB and SST over the tropical Pacific Ocean (140°W-70°W; 5°N-5°S). Thus, the ENSO-associated warming (cooling) of the central and eastern Pacific may favor years with relatively positive (negative) SMB over the SSI glaciers. According to Li et al. (2021), during El Niño events, there is typically a weakening of the ASL, which can induce cooling in the AP. However, depending on the type of ENSO it can influence the precipitation of the AP. During the eastern Pacific El Niño, precipitation decreases across the AP and the Amundsen-Bellingshausen seas, while during the central Pacific El Niño precipitation decreases mainly in the western AP and increases in the eastern AP (Chen et al., 2023). These different impacts on precipitation can inhibit the impact on the interannual SMB.

OLR over the west-central tropical Pacific (180°W-150°W; 28°S-5°S) also shows a weak but significant negative correlation with SMB. Specifically, negative OLR anomalies over the central tropical Pacific are related to positive SMB anomalies in SSI, similar to ENSO which are also associated with positive SMB anomalies over these islands. These OLR anomalies are accompanied by geopotential height anomalies at 300 hPa with the formation of a series of low, high, and low-pressure anomalies, as seen in Fig. 9c, extending from the tropics to the extratropics as a result of high convective activity over the central tropical Pacific. These negative OLR anomalies generate stationary Rossby wave trains propagating eastward and poleward, inducing atmospheric circulation anomalies affecting temperature, precipitation, and SMB in northern AP.

In winter, a deep low-pressure system extends from the Drake Passage to the Amundsen Sea and the western Weddell Sea (180°W-50°W), alongside a high-pressure system in the south-central Pacific Ocean (160°E-90°W; 60°S-30°S). These systems enhance westerly winds over southern South America (Fig. 10b), fostering cyclonic circulation over Drake Passage and precipitation over northern AP. Conversely, summer sees a high-pressure system over the Amundsen-Bellingshausen Sea and a low-pressure system in the southern Atlantic Ocean (Fig. 11a), promoting airflow from the Weddell Sea and regional cooling in the northern AP region.

4.6. *Correlation with large and regional scales indices*

Table 1 shows the correlations between different large-regional scale climate indices and the SMB, temperature, and snowfall from SSI_RACMO time series at annual, winter and summer timescales.

On an annual timescale, large-scale indices such as ENSO and SAM show low and statistically non-significant correlations with the SMB. In contrast, the DC-CPAC ($r = -0.32$, $p < 0.05$) index, also considered a large-scale index, shows moderate but statistically significant negative correlations. Regional indices over the Drake Passage show high and moderate negative correlations such as Z500-Drake ($r = -0.46$, $p < 0.05$) and SST-Drake ($r = -0.35$, $p < 0.05$), followed by the indices over the Amundsen-Bellingshausen and Weddell Seas, such as SST-ABSea (r

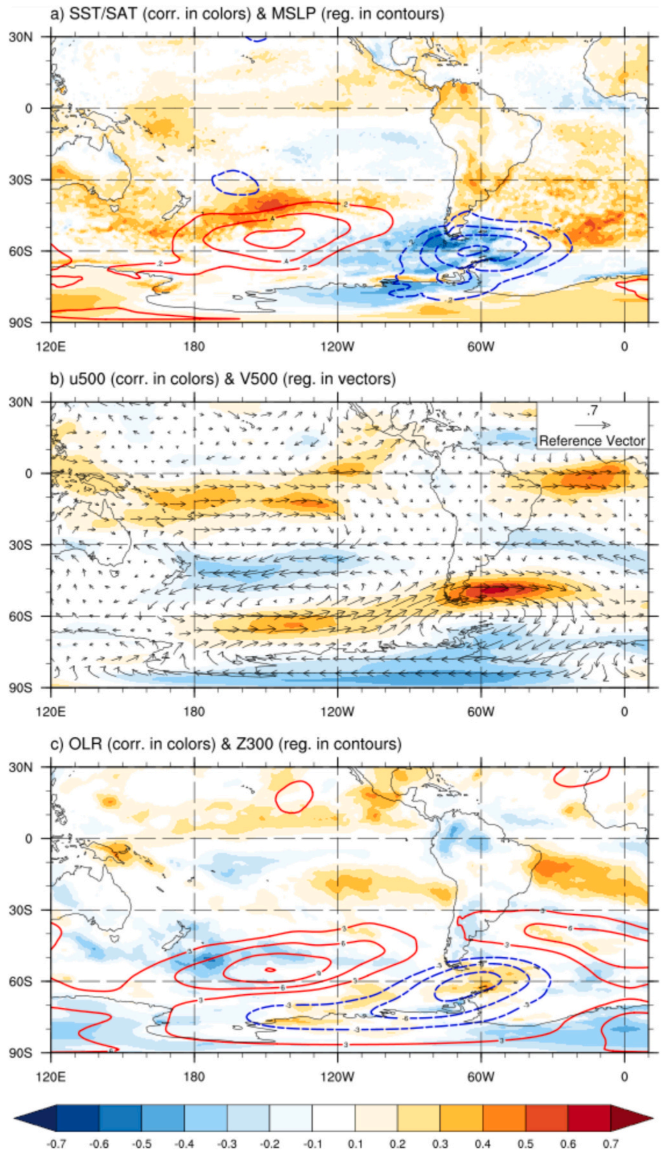

Fig. 9. Large-scale correlation and linear regression maps of the annual (April to March) SMB from SSI_RACMO time series with fields obtained from the ERA5 reanalysis. (a) Regression with the annual field of mean sea level pressure (contours in hPa per SD) and correlation with the annual field of sea surface temperature (colors over ocean) and near-surface air temperature (colors over land). (b) Regression with the annual field of horizontal wind at 500 hPa (vectors in m/s per SD) and correlation with the annual field of zonal wind at 500 hPa (colors). (c) Regression with the annual field of geopotential height at 300 hPa (contours in gpm per SD) and correlation with the annual field of outgoing longwave radiation (colors).

$= -0.36$, $p < 0.05$) and SST-WSea ($r = -0.30$, $p < 0.10$), respectively.

On the winter timescale, all of the large-scale indices show low and statistically non-significant correlations. Even several regional-scale indices associated with SST over the Amundsen-Bellingshausen, Weddell, and Drake Seas region show low correlations with the SMB. Only the regional Z500-Drake index shows a statistically moderate negative correlation ($r = -0.48$, $p < 0.05$) with the winter SMB.

On the summer timescale, large-scale indices show statistically significant positive and negative correlations such as El Niño 3 ($r = 0.37$, $p < 0.05$), El Niño 3.4 ($r = 0.36$, $p < 0.05$), El Niño 4 ($r = 0.29$, $p < 0.10$) and SAM ($r = -0.37$, $p < 0.05$) with the summer SMB. In addition to the large-scale indices, regional-scale indices show high and moderate negative and positive correlations such as Z500-Drake SST-Drake ($r = -0.60$, $p < 0.05$), ($r = -0.35$, $p < 0.05$), SST-WSea ($r = 0.43$, $p < 0.05$), SST-ABSea ($r = -0.41$, $p < 0.05$) and, ASL ($r = 0.33$, $p < 0.05$).

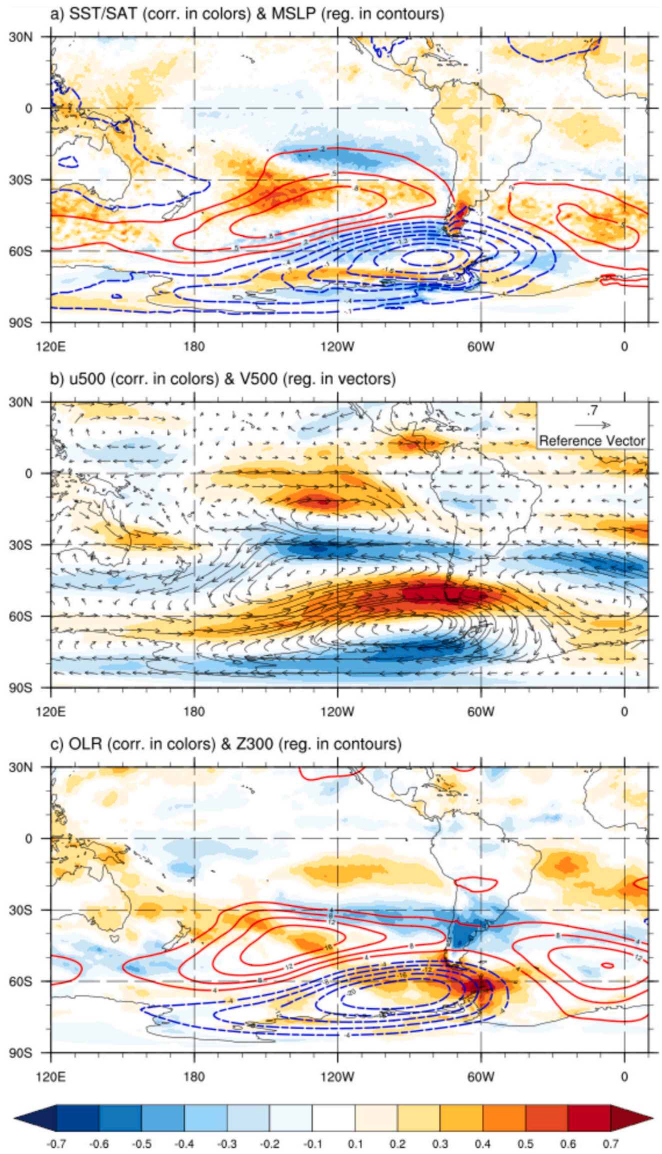

Fig. 10. The same as in Fig. 9 but for the winter (April to November).

Applying an exponential filter to the SMB and climate indices, we observed that Drake-related indices increase their correlation, e.g. Z500-Drake ($r = -0.53$, $p < 0.05$) and SST-Drake ($r = -0.42$, $p < 0.05$) at the annual timescale (Table S9), indicating that on a decadal scale the SSI SMB variability is also mainly related to anomalies in the atmospheric circulation and SST over the Drake region. Thus, from annual to decadal timescales, negative atmospheric pressure anomalies over the Drake are related to positive SSI SMB anomalies. Conversely, positive SST anomalies over Drake lead to negative SSI SMB anomalies. DC-CPAC also increases its correlation with the annual SMB (i.e., $r = -0.45$, $p < 0.05$), indicating that negative deep convection anomalies over the central tropical Pacific can drive positive SMB anomalies in SSI.

4.7. *Atmospheric rivers impact on SMB*

To investigate the impact of ARs on the SSI SMB, we analyzed the correlation between AR frequency and SMB from SSI_RACMO time series during winter and summer from 1980 to 2019 (Fig. 12). The results reveal two distinct impacts of ARs on the glacier SMB of the SSI

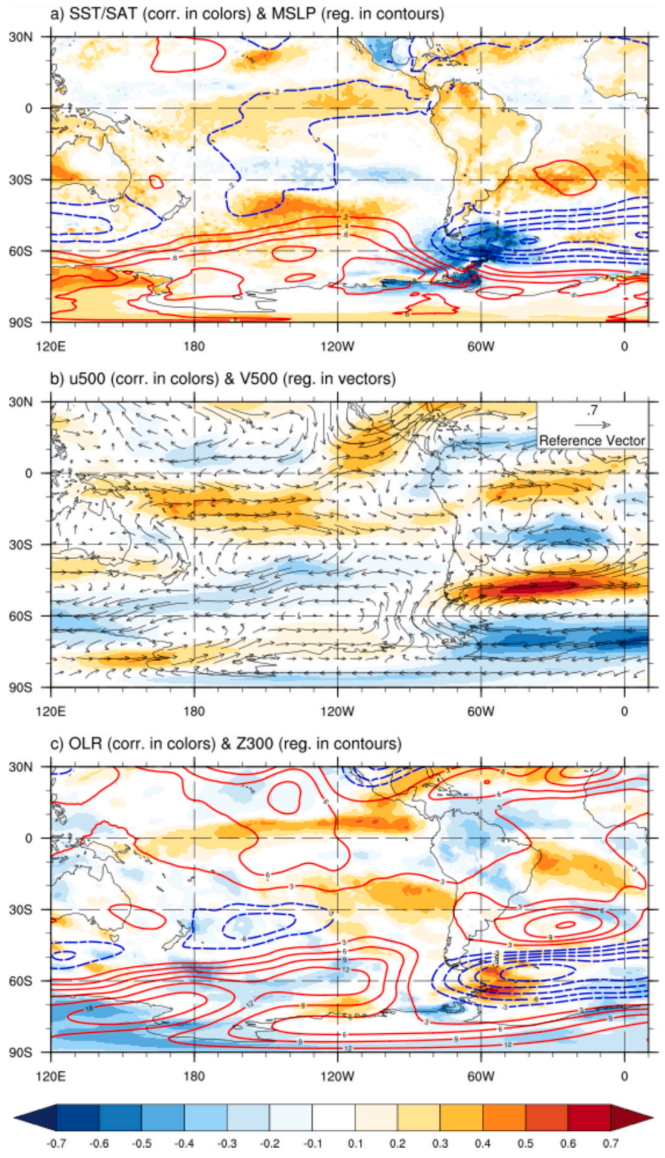
a) SST/SAT (corr. in colors) & MSLP (reg. in contours)

b) u500 (corr. in colors) & V500 (reg. in vectors)

c) OLR (corr. in colors) & Z300 (reg. in contours)

Fig. 11. The same as in Fig. 9 but for the summer (December to March).

(Table 2). Firstly, during winter (Fig. 12a), a positive and significant correlation between AR frequency and SMB is observed (r = 0.43, $p < 0.05$), indicating that ARs contribute to glacier accumulation through increased snowfall. However, higher correlations were observed when JJA ($r = 0.68$, $p < 0.05$) is considered only. Secondly, during summer (Fig. 12b), a negative and significant correlation between AR frequency and SMB is observed ($r = -0.37$, $p < 0.05$), suggesting that ARs intensify glacier melting in this season. Furthermore, when an exponential filter is applied to see decadal variations, the seasonal correlations increase (Table S10). These findings align with the regional temperature patterns: the winter temperatures during the ARs remain below the melting point, facilitating significant snowfall and glacier accumulation triggered by moisture transported by ARs. In contrast, summer temperatures approach or exceed the melting point, allowing ARs to amplify temperatures by means of sensible heat transport and enhance glacier melting. On an annual timescale, AR frequency and SMB present a negative but non-significant correlation ($r = -0.17$, non-significant), indicating that ARs contribute to glacier melting in this region.

For further analysis of the impact of ARs, we identified 20 cases associated with ARs based on the 99th percentile for winter snowfall and summer temperature from 1980 to 2019, using the daily GLAS_COSIPY time series. We then selected two cases out of these 20 with the highest positive and negative SMB values. These cases were observed on June 26, 1988, and January 23, 2006. Using ERA5 reanalysis data, we analyzed them to further illustrate the AR influences with the aid of the SMB, snowfall, rainfall, temperature, and sensible heat.

During the June 1988 case, axes with the same tracking ID in the life cycle show that AR had a northern-southern propagation axis, starting in the eastern Pacific Ocean and ending mainly in the northern AP. In addition, the AR in the life cycle had a northwest-southwest orientation (IVT direction of 107°) with a mean IVT of 394 kg m^{1} s^{1} and a length of 7866 km (Fig. 13b). A low-pressure system over the Drake Passage and a high-pressure system over the northern Weddell Sea were observed during the AR event, which allowed the transport of moisture from the Pacific Ocean to the northern AP. We highlight that the high-pressure system over the Weddell Sea is of great importance for the AR to enter perpendicularly over the northern AP. The MSLP composite analysis for the selected winter days (see Table S11) shows the same synoptic circulation pattern (Fig. 13a). During this AR period, the daily SMB was positive with a value of 30 mm w.e./day, the total precipitation was only snowfall (31 mm w.e./day), the surface temperature was below the melting point (−2.67 °C), and the sensible heat flux decreased moderately (14 W/m^{2}) compared to mean daily climatological (27 W/m^{2}).

During the January 2006 case, axes with the same track ID in the life cycle show that AR had a northern-southern propagation axis, starting in the South American continent and ending mainly in northern AP and the Weddell Sea, unlike the June 1988 case which started in the Pacific Ocean. AR in the life cycle had a northwest-southwest orientation (IVT direction of 115°) with a mean IVT of 177 kg m^{1} s^{1} and a length of 6540 km (Fig. 14b). A high-pressure system over the northern Weddell Sea was also observed during the AR event, which allowed the transport of continental air masses from South America to the northern AP and Weddell Sea. The high-pressure system during the summer is also observed in the MSLP composite analysis (Fig. 14a). During this AR

Table 1
Annual (April to March), winter (April to November) and summer (December to March) correlation analysis of surface mass balance (SMB), air temperature (Temp) and snowfall anomalies from SSI_RACMO time series with large-regional climatic indices from 1980 to 2019. Significance is indicated by an asterisk, where * ($p < 0.10$) and ** ($p < 0.05$).

	Annual correlation			Winter correlation			Summer correlation		
	SMB	TEMP	SNOWFALL	SMB	TEMP	SNOWFALL	SMB	TEMP	SNOWFALL
NIÑO 3	0.21	−0.34**	−0.08	−0.2	−0.24	−0.17	0.37**	−0.48**	0.25
NIÑO 3.4	0.21	−0.43**	−0.02	−0.2	−0.36**	−0.15	0.36**	−0.48**	0.24
NIÑO 4	0.13	−0.48**	−0.07	−0.23	−0.44**	−0.19	0.29*	−0.42**	0.21
DC-CPAC	−0.32**	−0.32**	−0.21	−0.19	−0.24	−0.13	−0.11	−0.05	−0.27*
SAM	−0.11	0.45**	0.21	0.06	0.54**	0.1	−0.37**	0.34**	−0.36**
ASL	0.17	−0.7**	−0.19	−0.19	−0.81**	−0.16	0.33**	−0.39**	0.22
SST-ABSea	−0.36**	0.26	−0.18	0.02	0.39**	−0.0	−0.41**	0.32**	−0.33**
SST-WSea	−0.3*	0.69**	−0.1	0.17	0.6**	0.14	−0.43**	0.53**	−0.01
Z500-Drake	−0.46**	0.28*	−0.54**	−0.48**	0.39**	−0.56**	−0.35**	0.21	−0.45**
SST-Drake	−0.35**	0.58**	−0.13	0.05	0.67**	0.06	−0.6**	0.5**	−0.24

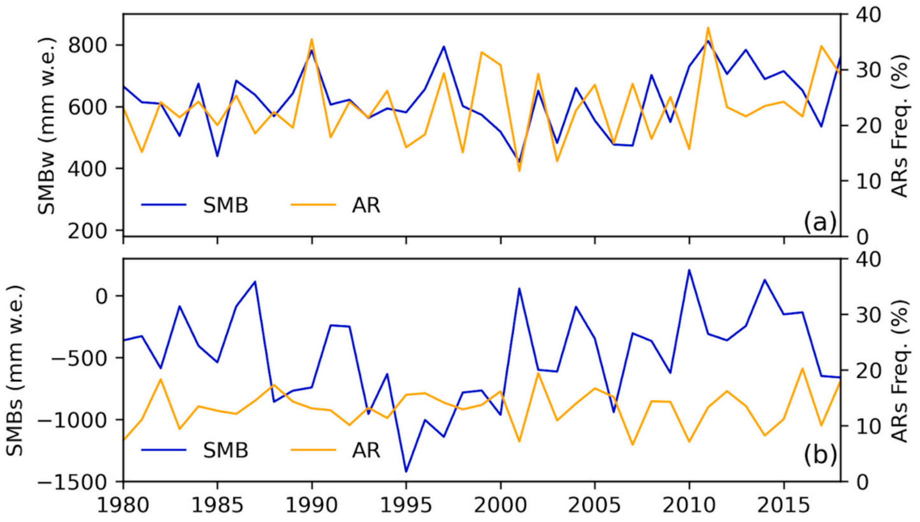

Fig. 12. (a) winter (April to November) and (b) summer (December to March) surface mass balance (blue line) from SSI_RACMO time series vs Atmospheric Rivers Frequency (orange line) from 1980 to 2019. (For interpretation of the references to colour in this figure legend, the reader is referred to the web version of this article.)

Table 2
Annual (April to March), winter (April to November) and summer (December to March) correlation for SMB, T2, and Snowfall from SSI_RACMO time series with ARs frequency from 1980 to 2019.

	Annual correlation	Winter correlation	Summer correlation	MAM	JJA	SON	DJF
SMB	−0.17	0.43**	−0.37**	−0.42**	0.68**	0.3*	−0.39**
TEMP	0.56**	0.67**	0.56**	0.75**	0.7**	0.61**	0.4**
SNOWFALL	0.21	0.42**	−0.22	−0.03	0.64**	0.22	−0.16

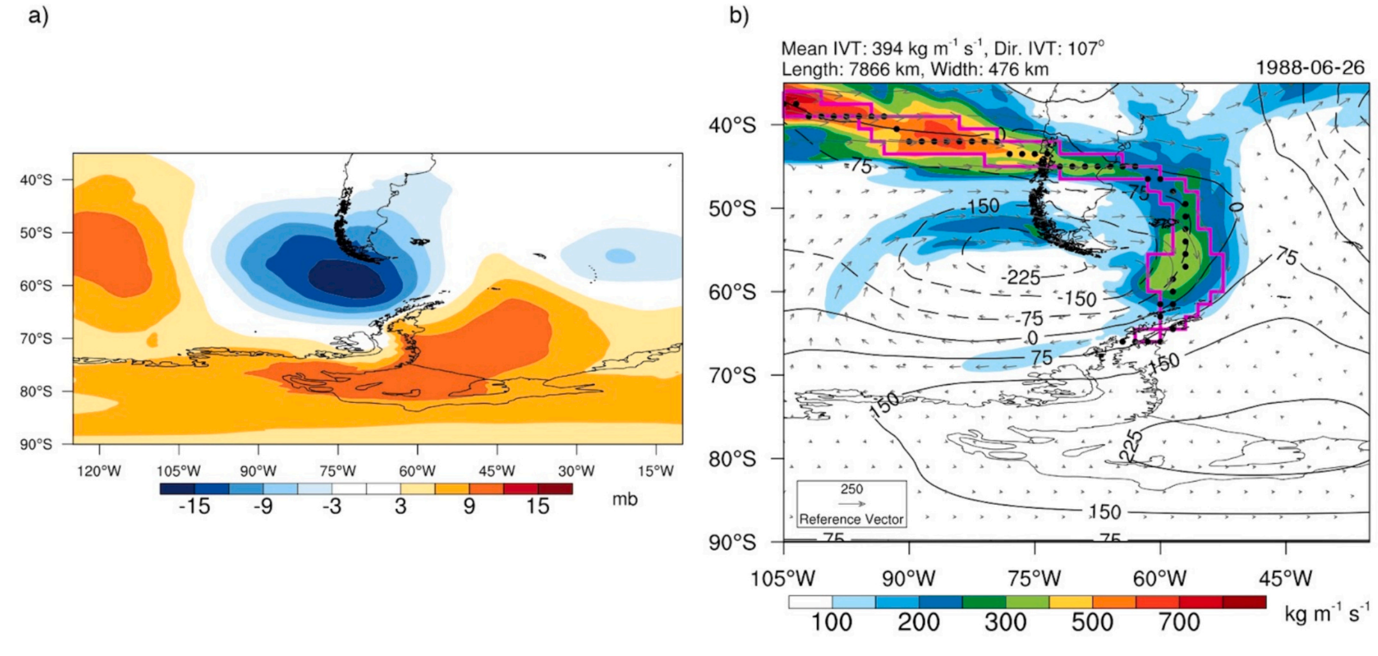

Fig. 13. (a) Composite daily anomalies MSLP for the selected AR days in winter (April to November) for the 1970–2020 period. (b) Characteristics of the extreme AR event detected on June 26, 1988, 12:00 UTC with IVT (shaded), IVT vectors, and 500 hPa geopotential height anomalies (contours) on that day. Black full circles show the axis of the AR.

event, the environmental conditions were favorable for a very negative SMB of −34 mm w.e./day, accompanied by positive temperature (3.57 °C), null total precipitation (snowfall + rainfall) and the sensible heat flux increased considerably (71 W/m^2) compared to mean daily climatological (27 W/m^2) (Table S11).

The analysis of these two extreme cases suggests that ARs can influence the SMB of glaciers in the SSI. On the one hand, during winter, ARs can contribute to large amounts of snowfall, which favors positive SMB. On the other hand, during summer, ARs increase the temperature of the northern AP, combined with null precipitation and high sensible

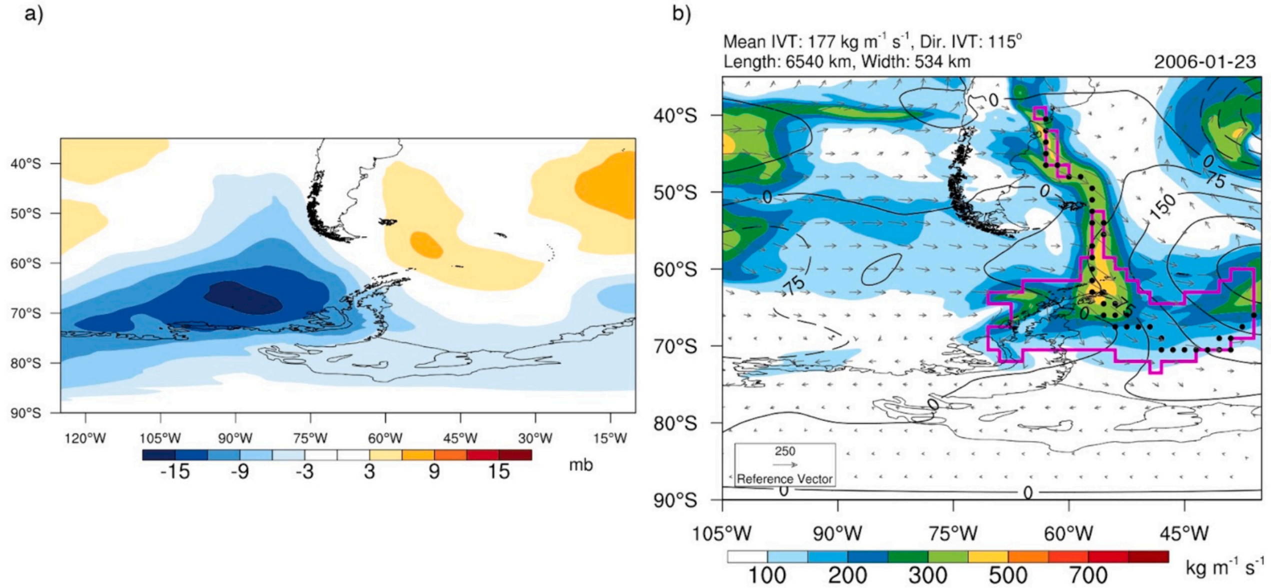

Fig. 14. (a) Composite daily anomalies in MSLP for the selected AR days in summer (December to March) for the 1970–2020 period. (b) Characteristics of the extreme AR event detected on January 23, 2006, 12:00 UTC with IVT (shaded), IVT vectors, and 500 hPa geopotential height anomalies (contours) on that day. Black full circles show the axis of the AR.

heat fluxes, creating favorable conditions for high melt rates and extremely negative SMB values.

Generally, the synoptic patterns of these two events are similar to the general pattern of the other extreme cases (20 cases, see Table S11), suggesting that the two selected main cases can be treated as representative of a larger sample size. During these events, there was typically a high-pressure center over the northern Weddell Sea (Figs. 13a and 14a) with a low-pressure center over the Drake Passage during winter or over the Amundsen-Bellingshausen Sea during summer.

5. Discussion

5.1. Glaciological modeling limitations

Despite uncertainties in the model and ERA5 climate data, PDD, COSIPY and RACMO effectively captured interannual and seasonal variability in glacier SMB. Sensitivity analysis revealed that COSIPY's key free parameters and uncertainties in meteorological inputs do not significantly affect the estimated SMB interannual variability (Tables S12, S13, and S14). Uncertainties in annual SMB variability may be associated with poor representation in the ERA5 reanalysis of precipitation fields across Antarctica (Roussel et al., 2020). Future atmospheric and glaciological modeling efforts should prioritize increasing the spatial resolution of the models to better represent local topography, orographic precipitation, and improve SMB modeling.

From the intercomparison of the different models (PDD, COSIPY, and RACMO), it is apparent that RACMO, despite its distributed configuration, does not exhibit significant changes in the interannual and seasonal variability of the SMB. Therefore, whether using a single-point or distributed model configuration does not impact the final glacier-wide SMB results for the SSI.

The SMB terminology is used to observe climate-related changes on glacier surfaces, excluding impacts from calving and/or frontal ablation processes (Cogley et al., 2010). Therefore, SMB is expected to vary little from glacier-to-glacier over short distances like those on the SSI. This is noted with high annual and seasonal correlation of the SMB observed between the three glaciers (Johnsons, Hurd and Bellingshausen), indicating that the SMB's annual and seasonal variability is consistent across these glaciers (Table S15). However, if we consider the geodetic mass balance, variations in mass balance are significant and can highly influence glacier-to-glacier mass changes over the SSI and northern AP (e.g., Shahateet et al., 2021; Seehaus et al., 2023).

Several factors limit the feasibility of distributed glaciological simulations for the studied glaciers. First, the absence of point SMB observations for these three glaciers makes a spatial evaluation of the models impossible. Second, Johnsons, Hurd, and Bellingshausen glaciers are very small, and a single grid from ERA5 or RACMO covers the entire glacier. Consequently, local-scale atmospheric processes are not well represented in ERA5, as evidenced by systematic errors in some atmospheric variables such as RH2, WS, and total precipitation (see Figs. S1 and S2). Third, since most glaciers in the SSI are in equilibrium with small or negligible annual mass balances, using the centroid as a reference point to simulate the SMB for the entire glacier is a reasonable approach. Finally, our simulation covered 51 years, and conducting very high-resolution simulations (both spatially and temporally) over this period would be prohibitively costly. For meaningful distributed glaciological simulations, it is essential to represent local atmospheric processes more accurately, possibly using models like the PWRF. Or, a mass balance method based on machine learning can (1) help improve the downscaling of the variables distributed in a glacier, (2) implicitly include glacial ice dynamics processes and (3) accelerate the execution of the model to run it at high resolution. However, such detailed modeling or use of machine learning falls outside the scope of our current study.

Our results align with other SMB studies in the region, though there are some differences in the findings. For example, Navarro et al. (2013) reported a mean SMB value of −50 ± 100 mm w.e./year for Hurd and Johnsons glaciers during the 2002–2011 period, while our findings show SMB values of 158 ± 320 mm w.e./year for SSI in the same period. Recently, Shahateet et al. (2021) reported a slightly negative mass balance (−106 ± 7 mm w.e.) for 2013–2017, contrasting our positive SMB (368 ± 272 mm w.e.). This difference may arise from glacier mass losses due to calving, a factor not included in the glaciological models used in this study. However, given the relative difference, it is reasonable to conclude that mass balance changes in this region are primarily driven by surface processes influenced by climate. Thus, although glacier-wide SMB is also influenced by glacier hypsometry and ice dynamics over the SSI, the influence of climate can still be extracted from it

(Zekollari et al., 2020; Bolibar et al., 2022).

5.2. SMB sensitivity and trends

Our sensitivity analysis reveals temperature, followed by snowfall, predominantly influences the interannual variability of these glacier's SMB (Tables S8 and S14). In contrast, solar radiation has a minimal effect. Correlation analysis indicates that ablation predominantly drives interannual SMB variations, followed by accumulation (Table S7). These findings are consistent with previous research highlighting the high sensitivity of these glaciers to small temperature fluctuations (e.g., Bintanja, 1995; Braun and Hock, 2004; Jonsell et al., 2012). For example, Jonsell et al. (2012) found that a temperature increase (decrease) of 0.5 °C implies an increase (decrease) in melting rates by approximately 56% (44%). This high sensitivity is attributed to the limited elevational range of these glaciers, resulting in temperatures near freezing during summer and thus a heightened response to minor temperature changes during melt seasons.

We identified a significant shift in the annual SMB trend around 1999. From 1980 to 1997, the SMB trend was significantly negative, indicating surface mass loss. However, from 1999 to 2014, the trend turned significantly positive, suggesting surface mass gain. However, a declining trend has emerged in recent years, from 2015 to 2019. These findings align with Oliva et al. (2017), who noted a slowed recession of marine and land-terminating glaciers in northern AP during the 2000s. This change in SMB trends aligns with documented regional temperature shifts, identified as the main driver of the glaciers' interannual variability (Turner et al., 2016, 2020; Oliva et al., 2017; Bozkurt et al., 2020; Bello et al., 2022). For example, Bello et al. (2022) reported warming and cooling periods before and after 2000 over King George Island, the largest island in SSI.

5.3. Relationship between large and regional climate indices and the SMB

We highlight that the Drake Passage significantly influences the annual SMB of SSI glaciers. At the annual timescale, regional climate indices such as Z500-Drake ($r = -0.46$, $p < 0.05$) and SST-Drake ($r = -0.35$, $p < 0.05$) show a moderate negative correlation with SMB. For winter, Z500-Drake ($r = -0.48$, $p < 0.05$) emerges as a potential influencing factor of SMB variability. During summer, a high and moderate negative correlation exists between SMB and SST-Drake ($r = -0.60$, $p < 0.05$) and Z500-Drake ($r = -0.35$, $p < 0.05$). We suggest that low-pressure anomalies over the Drake region (known as the Drake low) is a key driver of precipitation variability affecting both the Patagonia Icefields and SSI (Fig. 7a). Recent studies have indicated that the Drake low is a major controller of SMB variability over Patagonia Icefields (Carrasco-Escaff et al., 2023) and precipitation over the SSI (Torres et al., 2023). In addition, we speculate that Drake low can control regional temperature variability over the SSI due to the advection of cold air from Weddell to the northern AP (Fig. 8c), when it positions itself east of SSI. Our findings gain support through a correlation analysis of SMB between the Patagonia Icefields (time series from Carrasco-Escaff et al., 2023) and the SSI. We found a low correlation between SMB-Patagonia-Icefields and SMB-SSI during annual ($r = 0.30$, $p < 0.05$) and summer ($r = 0.18$, $p < 0.05$), while a high correlation is observed during winter ($r = 0.58$, $p < 0.05$). These results suggest winter SMB may be largely governed by the Drake low, whereas in summer and annually, the Drake low positioned over the northern Weddell Sea and DC-CPAC also play significant roles.

The annual SMB of SSI glaciers moderately depends on DC-CPAC climate indices, but shows less dependence on larger-scale climate patterns like SAM and ENSO. Interestingly, the summer SMB has a moderate dependence on ENSO, suggesting its significant influence during this period. Similar to Donat-Magnin et al. (2020), who indicated that the summer SMB and surface melting over the drainage basins of the Amundsen Sea glaciers, West Antarctica, are low influenced by ENSO. ENSO also shows a seasonally varied effect with a negative correlation in winter and a positive correlation in summer with SSI SMB (see Table 1). However, it shows a low dependence on DC-CPAC ($r = -0.05$, not-significant) but a moderate dependence on Z500-Drake ($r = -0.45$, $p < 0.05$). The correlation between summer surface melting on the SSI and DC-CPAC ($r = 0.13$, not-significant) exhibits low dependence. Compared to the results of Clem et al. (2022), who identified DC-CPAC as a major influence on surface melting at the Larsen C Ice Shelf in eastern AP, we suggest that in the complex climate of SSI, DC-CPAC's effects are likely overshadowed by other regional climate drivers, such as the low-pressure system over the Drake Passage.

Additionally, we used the observed and modeled SMB (COSIPY and RACMO) to relate to different climate indices (i.e., ENSO, SAM, ASL, Drake) from 2002 to 2019. The results indicate a similar correlation with these climate forcing indices (Tables S16 and S17). For example, ENSO and SAM show low correlations with the observed and modeled SMB (either COSIPY or RACMO). Whereas, the Drake low indices (i.e., Z500-Drake and SST-Drake) indicate high-moderate correlations with both observed and modeled SMB. These analyses suggest that, regardless of whether the SMB is observed or modeled, the results and conclusions remain consistent.

5.4. ARs' impact on SMB

The impact of ARs on the SMB in the SSI varies with the season. During the austral winter months, ARs from the Pacific Ocean, carrying warm and moist air, increase snowfall and contribute positively to the SMB. In contrast, during the austral summer, ARs originating from the Pacific Ocean and southern South America with warm air masses can enhance surface melting on glaciers in this region due increase of the sensible heat flux. The direction of ARs is also crucial in which west-to-east ARs impact the northern AP less than the central-south AP. In contrast, northwest-to-southwest ARs dominated by meridional winds affect the entire AP significantly. For instance, on January 23, 2006, a high-pressure system over the northern Weddell Sea led to a high ablation rate in the SSI. This pattern aligns with findings by Zou et al. (2022), who noted the northern AP's vulnerability to ARs combined with atmospheric blocks over the Weddell Sea. Our study emphasizes the role of low-pressure systems in the Drake Passage and the Weddell Sea in enhancing SMB, whereas high-pressure systems in these areas can cause significant SMB reduction. Consistent with these results, Braun et al. (2001) reported that the SSI's highest surface melt rates (up to 20 mm w.e./day) occurred during northwestern advection events linked to low-pressure over the Bellingshausen Sea. They also found that easterly and southerly cold, dry air masses, influenced by high-pressure over the AP and low-pressure over the Weddell Sea, had minimal impact on ablation rates.

In addition, during summer, the presence of these high- or low-pressure systems can modulate the frequency of snowfall or rainfall over northern AP (Wang et al., 2021). When the low-pressure center is located over western Drake with a high-pressure system over the Falkland Islands, it can favor the frequency of rainfall over northern AP. When the low-pressure center is located west-central over Drake, accompanied by a low-pressure system over the Weddell Sea, it may favor more frequent snowfall over the SSI.

5.5. Tropical forcings on the SSI environmental conditions

The interannual variability of SMB in the SSI is largely governed by surface and atmospheric pressure anomalies and SST anomalies over the Drake Passage, influenced by tropical forces like ENSO and DC-CPAC. It is plausible to suggest that tropical forcings alter sea surface and atmospheric conditions at regional scales over the AP, affecting the SSI's SMB. Subsequently, these regional changes strongly control the SMB of the SSI. While our study does not delve into the specific mechanisms behind Drake pressure anomalies, they're probably impacted by tropical forces and regional temperature variations (e.g., Hoskins and Karoly, 1981; Karoly, 1989; Carrasco-Escaff et al., 2023; Clem et al., 2022; Gorodetskaya et al., 2023). Studies like Carrasco-Escaff et al. (2023) suggest that Drake low's formation is sensitive to SST anomalies in the tropical Pacific, influencing precipitation and SMB in the Patagonia Icefields. Recent findings, indicate complex interactions, like Rossby waves influencing the AP's climate through synoptic scale circulation anomalies such as intensification of ASL and strengthened high pressure over Drake Passage (e.g., Rondanelli et al., 2019; Clem et al., 2022; Gorodetskaya et al., 2023). These insights highlight the need for further research to fully understand the teleconnections affecting the Drake atmospheric circulation anomalies.

We found that at the interannual scale, ASL is strongly related to SAM ($r = -0.74$, $p < 0.05$) (Table S18). However, at the decadal scale, ASL shows a stronger relationship with El Niño 4 ($r = 0.65$, $p < 0.05$) (Table S19), indicating that positive surface temperature anomalies over the tropics lead to positive ASL anomalies. According to Li et al. (2021), during El Niño events, there is typically a weakening of the ASL, which can induce cooling in the AP of up to 1.5 °C and positive anomalies in sea ice concentration of up to 10–20% in the vicinity of the Amundsen, Bellingshausen, and Weddell Seas. We also found that the Z500-Drake index shows low correlation with the large-scale climate indices (ENSO and SAM) but moderate and significant correlation with SST-ABSea ($r = 0.38$, $p < 0.05$). This would indicate that pressure anomalies over Drake can be associated with sea surface temperature anomalies over the Bellingshausen Sea. However, further analysis of these relationships is needed to identify which drivers influence the atmospheric pressure anomalies over Drake.

6. Conclusions

This study explored the climatic influences on the SMB of SSI glaciers on seasonal and interannual timescales. Employing the RACMO and COSIPY glaciological models, we obtained robust SMB time series for SSI glaciers. We then analyzed detrended SMB anomaly time series against climate variables to understand their relationship with key atmospheric modes of variability at the interannual timescale. Additionally, we assessed the impact of AR events on the seasonal SMB of SSI glaciers, shedding light on various climate processes at different scales affecting SMB. Key conclusions include:

- **Interannual SMB Variability:** Near-surface temperature and precipitation mainly drive the interannual variability of SSI glaciers' SMB, while insolation has minimal impact.
- **Local-Scale Conditions:** Years with higher-than-average SMB correlate with increased annual accumulation and reduced summer ablation, linked to more annual precipitation and lowered summer near-surface temperatures. Lower-than average SMB years show the opposite conditions.
- **Break in SMB Trends:** A notable shift in the SMB trend aligns with regional warming and cooling trends of the AP. A significant negative SMB trend was observed in the 1970–1997 period, followed by a significant positive trend in the 1999–2014 period. Since 2015, there has been a trend towards extremely negative SMB rates.
- **Positive/Negative SMB years:** Positive SMB years are associated with low-pressure systems over Drake Passage (known as the Drake low), enhancing winter snowfall and cooling the northern AP in summer. Negative SMB years are linked to high-pressure systems over the Weddell Sea in summer, leading to increased surface ablation due to meridional winds.
- **Climate Variability Modes:** Interannual SMB variability shows little correlation with major climate modes like SAM and ENSO, though these may moderately influence summer SMB. ENSOs' effects on SMB vary seasonally. Interannually, ESNO positive (during El Niño events) and DC-CPAC (negative anomalies) are associated by slightly positive SMB anomalies in SSI.
- **AR Events Impact:** ARs' effects on SMB vary seasonally. Winter ARs typically lead to positive SMB conditions, while summer ARs can have a negative impact. Typically, these ARs feature low pressure anomalies over the Amundsen-Bellingshausen Sea in summer and the Drake Passage in winter, accompanied by high pressure over the Weddell Sea, leading to prevalent meridional winds.

Our study gives new insights into the complex interplay between current climate processes and cryospheric dynamics in island glaciers on the northern Antarctic Peninsula. We underscore that the interannual SMB variability in these glaciers is largely responsive to SST anomalies and surface and atmospheric pressure anomalies over the Drake Passage and northern Weddell Sea. Specifically, negative atmospheric pressure anomalies over the Drake Passage are correlated with positive SSI SMB anomalies. Conversely, positive SST anomalies over the Drake Passage result in negative SSI SMB anomalies. Furthermore, we highlighted the need for further glacier-climate studies to delve into the seasonal and intraseasonal impacts of various climate forcings and ARs on the AP environment, particularly on small-scale glaciers along the coastal zone.

CRediT authorship contribution statement

Christian Torres: Conceptualization, Methodology, Software, Validation, Writing – original draft. **Deniz Bozkurt:** Conceptualization, Methodology, Software, Writing – review & editing. **Tomás Carrasco-Escaff:** Software, Writing – review & editing. **Jordi Bolibar:** Methodology, Writing – review & editing. **Jorge Arigony-Neto:** Conceptualization, Supervision, Writing – review & editing.

Declaration of competing interest

The authors declare that they have no known competing financial interests or personal relationships that could have appeared to influence the work reported in this paper.

Data availability

Data will be made available on request.

Acknowledgments

We express gratitude to the Aperfeiçoamento de Pessoal de Nível Superior (CAPES) for supporting the Graduate Program in Oceanology at Universidade Federal do Rio Grande (FURG). The first author also acknowledges CAPES for the PhD scholarship. Special thanks to ECMWF for providing ERA5 data and JM van Wessem for RACMO data. We also appreciate Francisco Navarro for insightful discussions on this research. The data (KOPRI-KPDC-00000960) from King Sejong Station used in this work was provided by the Korea Polar Research Institute. Powered@NLHPC: This research/thesis was partially supported by the supercomputing infrastructure of the NLHPC (CCSS210001). DB acknowledges support from ANID-FONDECYT-1240190, ANID-FONDAP-1523A0002, and COPAS COASTAL ANID FB210021. Thanks also to the support of the projects CNPq 465680/2014-3 and FAPERGS 17/2551-0000518-0 (INCT da Criosfera), CNPq-Universal 407653/2023-6, and CAPES-CLIMAT AMSUD 88881.878909/2023-01 (TROPIPOLAR-GLASCLIM). Finally, we extend our thanks for the SCAR fellowships (https://www.scar.org/general-scar-news/2022-scar-fellows/) that enabled the first author to conduct a research exchange at the University of Valparaíso, Chile.

Appendix A. Supplementary data

Supplementary data to this article can be found online at https://doi.org/10.1016/j.gloplacha.2024.104506.

References

Arndt, A., Scherer, D., Schneider, C., 2021. Atmosphere driven mass-balance sensitivity of Halji Glacier, Himalayas. Atmosphere 12 (4), 426. https://doi.org/10.3390/atmos12040426.

Bello, C., Suarez, W., Lavado-Casimiro, W., 2022. Trends and space–time patterns of near-surface temperatures on Maxwell Bay, King George Island, Antarctica. Int. J. Climatol. 42 (14), 7426–7442. https://doi.org/10.1002/joc.7661.

Bergstra, J., Bengio, Y., 2012. Random search for hyper-parameter optimization. J. Mach. Learn. Res. 13 (2).

Bintanja, R., 1995. The local surface energy balance of the Ecology Glacier, King George Island, Antarctica: measurements and modelling. Antarct. Sci. 7 (3), 315–325. https://doi.org/10.1017/S0954102095000435.

Bolibar, J., Rabatel, A., Gouttevin, I., Zekollari, H., Galiez, C., 2022. Nonlinear sensitivity of glacier mass balance to future climate change unveiled by deep learning. Nat. Commun. 13 (1), 409. https://doi.org/10.1038/s41467-022-28033-0.

Bozkurt, D., Bromwich, D.H., Carrasco, J., Hines, K.M., Maureira, J.C., Rondanelli, R., 2020. Recent near-surface temperature trends in the Antarctic Peninsula from observed, reanalysis and regional climate model data. Adv. Atmos. Sci. 37, 477–493. https://doi.org/10.1007/s00376-020-9183-x.

Bozkurt, D., Bromwich, D.H., Carrasco, J., Rondanelli, R., 2021. Temperature and precipitation projections for the Antarctic Peninsula over the next two decades: contrasting global and regional climate model simulations. Clim. Dyn. 56 (11−12), 3853–3874. https://doi.org/10.1007/s00382-021-05667-2.

Braithwaite, R.J., 1995. Positive degree-day factors for ablation on the Greenland ice sheet studied by energy-balance modelling. J. Glaciol. 41 (137), 153–160. https://doi.org/10.3189/S0022143000017846.

Braun, M., Hock, R., 2004. Spatially distributed surface energy balance and ablation modelling on the ice cap of King George Island (Antarctica). Glob. Planet. Chang. 42 (1–4), 45–58. https://doi.org/10.1016/j.gloplacha.2003.11.010.

Braun, M., Saurer, H., Vogt, S., Simões, J.C., Goßmann, H., 2001. The influence of large-scale atmospheric circulation on the surface energy balance of the King George Island ice cap. Int. J. Climatol. 21 (1), 21–36. https://doi.org/10.1002/joc.563.

Bromwich, D.H., Nicolas, J.P., Monaghan, A.J., Lazzara, M.A., Keller, L.M., Weidner, G. A., Wilson, A.B., 2013. Central West Antarctica among the most rapidly warming regions on Earth. Nat. Geosci. 6 (2), 139–145. https://doi.org/10.1038/ngeo1671.

Carrasco, J.F., Cordero, R.R., 2020. Analyzing precipitation changes in the northern tip of the Antarctic peninsula during the 1970–2019 period. Atmosphere 11 (12), 1270. https://doi.org/10.3390/atmos11121270.

Carrasco, J.F., Bozkurt, D., Cordero, R.R., 2021. A review of the observed air temperature in the Antarctic Peninsula. Did the warming trend come back after the early 21st hiatus? Polar Sci. 28, 100653 https://doi.org/10.1016/j.polar.2021.100653.

Carrasco-Escaff, T., Rojas, M., Garreaud, R.D., Bozkurt, D., Schaefer, M., 2023. Climatic control of the surface mass balance of the Patagonian Icefields. Cryosphere 17 (3), 1127–1149. https://doi.org/10.5194/tc-17-1127-2023.

Chen, X., Li, S., Zhang, C., 2023. Distinct impacts of two kinds of El Niño on precipitation over the Antarctic Peninsula and West Antarctica in austral spring. Atmos. Ocean. Sci. Lett. 16 (5), 100387 https://doi.org/10.1016/j.aosl.2023.100387.

Clem, K.R., Fogt, R.L., 2013. Varying roles of ENSO and SAM on the Antarctic Peninsula climate in austral spring. J. Geophys. Res. Atmos. 118 (20), 11–481. https://doi.org/10.1002/jgrd.50860.

Clem, K.R., Renwick, J.A., McGregor, J., Fogt, R.L., 2016. The relative influence of ENSO and SAM on Antarctic Peninsula climate. J. Geophys. Res. Atmos. 121 (16), 9324–9341. https://doi.org/10.1002/2016JD025305.

Clem, K.R., Bozkurt, D., Kennett, D., King, J.C., Turner, J., 2022. Central tropical Pacific convection drives extreme high temperatures and surface melt on the Larsen C Ice Shelf, Antarctic Peninsula. Nat. Commun. 13 (1), 3906. https://doi.org/10.1038/s41467-022-31119-4.

Cogley, J.G., Arendt, A.A., Bauder, A., Braithwaite, R.J., Hock, R., Jansson, P., Zemp, M., 2010. Glossary of Glacier Mass Balance and Related Terms.

Cook, A.J., Holland, P.R., Meredith, M.P., Murray, T., Luckman, A., Vaughan, D.G., 2016. Ocean forcing of glacier retreat in the western Antarctic Peninsula. Science 353 (6296), 283–286. https://doi.org/10.1126/science.aae0017.

Costi, J., Arigony-Neto, J., Braun, M., Mavlyudov, B., Barrand, N.E., Da Silva, A.B., Simoes, J.C., 2018. Estimating surface melt and runoff on the Antarctic Peninsula using ERA-Interim reanalysis data. Antarct. Sci. 30 (6), 379–393. https://doi.org/10.1017/S0954102018000391.

da Rosa, K.K., Perondi, C., Veettil, B.K., Auger, J.D., Simões, J.C., 2020. Contrasting responses of land-terminating glaciers to recent climate variations in King George Island, Antarctica. Antarct. Sci. 32 (5), 398–407. https://doi.org/10.1017/S0954102020000279.

Ding, Q., Steig, E., Battisti, D., Kuttel, M., 2011. Winter warming in West Antarctica caused by central tropical Pacific warming. Nat. Geosci. 4, 398–403. https://doi.org/10.1038/ngeo1129.

Donat-Magnin, M., Jourdain, N.C., Gallée, H., Amory, C., Kittel, C., Fettweis, X., Agosta, C., 2020. Interannual variability of summer surface mass balance and surface melting in the Amundsen sector, West Antarctica. Cryosphere 14 (1), 229–249. https://doi.org/10.5194/tc-14-229-2020.

Dong, Y., Zhao, J., Li, C., Liao, M., 2022. Gapless-REMA100: a gapless 100-m reference elevation model of Antarctica with voids filled by multi-source DEMs. ISPRS J. Photogramm. Remote Sens. 186, 70–82. https://doi.org/10.1016/j.isprsjprs.2022.01.024.

Falk, U., López, D.A., Silva-Busso, A., 2018. Multi-year analysis of distributed glacier mass balance modelling and equilibrium line altitude on King George Island, Antarctic Peninsula. Cryosphere 12 (4), 1211–1232. https://doi.org/10.5194/tc-12-1211-2018.

Fogt, R.L., Marshall, G.J., 2020. The Southern Annular Mode: variability, trends, and climate impacts across the Southern Hemisphere. WIREs Clim. Change 11 (4). https://doi.org/10.1002/wcc.652.

Fogt, R.L., Bromwich, D.H., Hines, K.M., 2011. Understanding the SAM influence on the South Pacific ENSO teleconnection. Clim. Dyn. 36 (7–8), 1555–1576. https://doi.org/10.1007/s00382-010-0905-0.

Fogt, R.L., Sleinkofer, A.M., Raphael, M.N., Handcock, M.S., 2022. A regime shift in seasonal total Antarctic Sea ice extent in the twentieth century. Nat. Clim. Chang. 12 (1), 54–62. https://doi.org/10.1038/s41558-021-01254-9.

Gallée, H., Schayes, G., 1994. Development of a three-dimensional meso-γ primitive equation model: katabatic winds simulation in the area of Terra Nova Bay, Antarctica. Mon. Weather Rev. 122 (4), 671–685. https://doi.org/10.1175/1520-0493(1994)122<0671:DOATDM>2.0.CO;2.

Gonzalez, S., Vasallo, F., Recio-Blitz, C., Guijarro, J.A., Riesco, J., 2018. Atmospheric patterns over the Antarctic Peninsula. J. Clim. 31 (9), 3597–3608. https://doi.org/10.1175/JCLI-D-17-0598.1.

Gorodetskaya, I.V., Durán-Alarcón, C., González-Herrero, S., et al., 2023. Record-high Antarctic Peninsula temperatures and surface melt in February 2022: a compound event with an intense atmospheric river. Npj Clim. Atmos. Sci. 6, 202. https://doi.org/10.1038/s41612-023-00529-6.

Gossart, A., Helsen, S., Lenaerts, J.T.M., Broucke, S.V., Van Lipzig, N.P.M., Souverijns, N., 2019. An evaluation of surface climatology in state-of-the-art reanalyses over the Antarctic ice sheet. J. Clim. 32 (20), 6899–6915. https://doi.org/10.1175/JCLI-D-19-0030.1.

Guan, B., Waliser, D.E., 2019. Tracking atmospheric rivers globally: spatial distributions and temporal evolution of life cycle characteristics. J. Geophys. Res. Atmos. 124 (23), 12523–12552. https://doi.org/10.1029/2019JD031205.

Hersbach, H., Bell, B., Berrisford, P., Hirahara, S., Horanyi, A., Munoz-Sabater, J., et al., 2020. The ERA5 global reanalysis. Q. J. R. Meteorol. Soc. 146 (730), 1999–2049. https://doi.org/10.1002/qj.3803.

Hillebrand, F.L., Bremer, U.F., Arigony-Neto, J., da Rosa, C.N., Mendes Jr., C.W., Costi, J., Schardong, F., 2021. Comparison between atmospheric reanalysis models ERA5 and ERA-interim at the North Antarctic Peninsula region. Ann. Am. Assoc. Geogr. 111 (4), 1147–1159. https://doi.org/10.1080/24694452.2020.1807308.

Hines, K.M., Bromwich, D.H., 2008. Development and testing of Polar Weather Research and Forecasting (WRF) model. Part I: Greenland ice sheet meteorology. Mon. Weather Rev. 136 (6), 1971–1989. https://doi.org/10.1175/2007MWR2112.1.

Hosking, J.S., Orr, A., Bracegirdle, T.J., Turner, J., 2016. Future circulation changes off West Antarctica: sensitivity of the Amundsen Sea Low to projected anthropogenic forcing. Geophys. Res. Lett. 43 (1), 367–376. https://doi.org/10.1002/2015GL067143.

Hoskins, B.J., Karoly, D.J., 1981. The steady linear response of a spherical atmosphere to thermal and orographic forcing. J. Atmos. Sci. 38 (6), 1179–1196. https://doi.org/10.1175/1520-0469(1981)038<1179:TSLROA>2.0.CO;2.

Jonsell, U.Y., Navarro, F.J., Bañón, M., Lapazaran, J.J., Otero, J., 2012. Sensitivity of a distributed temperature-radiation index melt model based on AWS observations and surface energy balance fluxes, Hurd Peninsula glaciers, Livingston Island, Antarctica. Cryosphere 6 (3), 539–552. https://doi.org/10.5194/tc-6-539-2012.

Karoly, D.J., 1989. Southern hemisphere circulation features associated with El Niño-Southern Oscillation events. J. Clim. 2 (11), 1239–1252. https://doi.org/10.1175/1520-0442(1989)002<1239:SHCFAW>2.0.CO;2.

Kerr, R., Mata, M.M., Mendes, C.R.B., Secchi, E.R., 2018. Northern Antarctic Peninsula: a marine climate hotspot of rapid changes on ecosystems and ocean dynamics. Deep-Sea Res. II Top. Stud. Oceanogr. 149, 4–9. https://doi.org/10.1016/j.dsr2.2018.05.006.

King, M.A., Lyu, K., Zhang, X., 2023. Climate variability a key driver of recent Antarctic ice-mass change. Nat. Geosci. 16 (12), 1128–1135. https://doi.org/10.1038/s41561-023-01317-w.

Knap, W.H., Oerlemans, J., Cabée, M., 1996. Climate sensitivity of the ice cap of king George Island, South Shetland Islands, Antarctica. Ann. Glaciol. 23, 154–159. https://doi.org/10.3189/S0260305500013380.

Li, X., Cai, W., Meehl, G.A., Chen, D., Yuan, X., Raphael, M., Song, C., 2021. Tropical teleconnection impacts on Antarctic climate changes. Nat. Rev. Earth Environ. 2 (10), 680–698. https://doi.org/10.1038/s43017-021-00204-5.

Ligtenberg, S.R.M., Helsen, M.M., Van den Broeke, M.R., 2011. An improved semi-empirical model for the densification of Antarctic firn. Cryosphere 5 (4), 809–819. https://doi.org/10.5194/tc-5-809-2011.

Marshall, G.J., 2003. Trends in the Southern Annular Mode from observations and reanalyses. J. Clim. 16 (24), 4134–4143. https://doi.org/10.1175/1520-0442(2003)016<4134:TITSAM>2.0.CO;2.

Marshall, G.J., 2007. Half-century seasonal relationships between the Southern Annular Mode and Antarctic temperatures. Int. J. Climatol. 27 (3), 373–383. https://doi.org/10.1002/joc.1407.

Mölg, T., Maussion, F., Yang, W., Scherer, D., 2012. The footprint of Asian monsoon dynamics in the mass and energy balance of a Tibetan glacier. Cryosphere 6 (6), 1445–1461. https://doi.org/10.5194/tc-6-1445-2012.

Molina, C., Navarro, F.J., Calvet, J., García-Sellés, D., Lapazaran, J.J., 2007. Hurd Peninsula glaciers, Livingston Island, Antarctica, as indicators of regional warming: ice-volume changes during the period 1956–2000. Ann. Glaciol. 46, 43–49. https://doi.org/10.3189/172756407782871765.

Navarro, F.J., Jonsell, U.Y., Corcuera, M.I., Martín-Español, A., 2013. Decelerated mass loss of Hurd and Johnsons Glaciers, Livingston Island, Antarctic Peninsula. J. Glaciol. 59 (213), 115–128. https://doi.org/10.3189/2013JoG12J144.

Navarro, F., Recio-Blitz, C., Rodríguez-Cielos, R., Otero, J., Shahateet, K., De Andrés, E., Muñoz-Hermosilla, J.M., 2023. Surface mass balance monitoring of the peripheral glaciers of the Antarctic Peninsula in the context of regional climate change. Ann. Glaciol. 1–6. https://doi.org/10.1017/aog.2023.18.

Oliva, M., Navarro, F., Hrbáček, F., Hernandéz, A., Nývlt, D., Pereira, P., Trigo, R., 2017. Recent regional climate cooling on the Antarctic Peninsula and associated impacts on the cryosphere. Sci. Total Environ. 580, 210–223. https://doi.org/10.1016/j.scitotenv.2016.12.030.

Osmanoğlu, B., Braun, M., Hock, R., Navarro, F.J., 2013. Surface velocity and ice discharge of the ice cap on King George Island, Antarctica. Ann. Glaciol. 54 (63), 111–119. https://doi.org/10.3189/2013AoG63A517.

Pasik, M., Bakuła, K., Różycki, S., Ostrowski, W., Kowalska, M.E., Fijałkowska, A., Osińska-Skotak, K., 2021. Glacier geometry changes in the western shore of Admiralty Bay, King George Island over the last decades. Sensors 21 (4), 1532. https://doi.org/10.3390/s21041532.

Pętlicki, M., Sziło, J., MacDonell, S., Vivero, S., Bialik, R.J., 2017. Recent deceleration of the ice elevation change of Ecology Glacier (King George Island, Antarctica). Remote Sens. 9 (6), 520. https://doi.org/10.3390/rs9060520.

Pudełko, R., Angiel, P.J., Potocki, M., Jędrejek, A., Kozak, M., 2018. Fluctuation of glacial retreat rates in the eastern part of Warszawa Icefield, King George Island, Antarctica, 1979–2018. Remote Sens. 10 (6), 892. https://doi.org/10.3390/rs10060892.

RGI Consortium, 2017. Randolph Glacier Inventory - a Dataset of Global Glacier Outlines, Version 6 [Data Set]. National Snow and Ice Data Center, Boulder, Colorado USA.

Rondanelli, R., Hatchett, B., Rutllant, J., Bozkurt, D., Garreaud, R., 2019. Strongest MJO on record triggers extreme Atacama rainfall and warmth in Antarctica. Geophys. Res. Lett. 46 (6), 3482–3491. https://doi.org/10.1029/2018GL081475.

Roussel, M.L., Lemonnier, F., Genthon, C., Krinner, G., 2020. Brief communication: evaluating Antarctic precipitation in ERA5 and CMIP6 against CloudSat observations. Cryosphere 14 (8), 2715–2727. https://doi.org/10.5194/tc-14-2715-2020.

Rückamp, M., Blindow, N., Suckro, S., Braun, M., Humbert, A., 2010. Dynamics of the ice cap on King George Island, Antarctica: field measurements and numerical simulations. Ann. Glaciol. 51 (55), 80–90. https://doi.org/10.3189/172756410791392817.

Rückamp, M., Braun, M., Suckro, S., Blindow, N., 2011. Observed glacial changes on the King George Island ice cap, Antarctica, in the last decade. Glob. Planet. Chang. 79 (1–2), 99–109. https://doi.org/10.1016/j.gloplacha.2011.06.009.

Sauter, T., Arndt, A., Schneider, C., 2020. COSIPY v1. 3–an open-source coupled snowpack and ice surface energy and mass balance model. Geosci. Model Dev. 13 (11), 5645–5662. https://doi.org/10.5194/gmd-13-5645-2020.

Seehaus, T., Sommer, C., Dethinne, T., Malz, P., 2023. Mass changes of the northern Antarctic Peninsula ice sheet derived from repeat bi-static synthetic aperture radar acquisitions for the period 2013–2017. Cryosphere 17 (11). https://doi.org/10.5194/tc-17-4629-2023.

Shahateet, K., Seehaus, T., Navarro, F., Sommer, C., Braun, M., 2021. Geodetic mass balance of the South Shetland Islands ice caps, Antarctica, from differencing TanDEM-X DEMs. Remote Sens. 13 (17), 3408. https://doi.org/10.3390/rs13173408.

Silva, A.B., Arigony-Neto, J., Braun, M.H., Espinoza, J.M.A., Costi, J., Jaña, R., 2020. Spatial and temporal analysis of changes in the glaciers of the Antarctic Peninsula. Glob. Planet. Chang. 184, 103079 https://doi.org/10.1016/j.gloplacha.2019.103079.

Simões, J.C., Dani, N., Bremer, U.F., Aquino, F.E., Arigony Neto, J., 2004. Small Cirque Glaciers Retreat on Keller Peninsula, Admiralty Bay, King George Island, Antarctica. https://doi.org/10.31789/pab.v4n1.005.

Sobota, I., Kejna, M., Araźny, A., 2015. Short-term mass changes and retreat of the Ecology and Sphinx glacier system, King George Island, Antarctic Peninsula. Antarct. Sci. 27 (5), 500–510. https://doi.org/10.1017/S0954102015000188.

Temme, F., Farías-Barahona, D., Seehaus, T., Jaña, R., Arigony-Neto, J., Gonzalez, I., Fürst, J.J., 2023. Strategies for regional modeling of surface mass balance at the Monte Sarmiento Massif, Tierra del Fuego. Cryosphere 17 (6), 2343–2365.

Tetzner, D., Thomas, E., Allen, C., 2019. A validation of ERA5 reanalysis data in the Southern Antarctic Peninsula—Ellsworth land region, and its implications for ice core studies. Geosciences 9 (7), 289. https://doi.org/10.3390/geosciences9070289.

Torres, C., Bozkurt, D., Arigony-Neto, J., 2023. Large-scale and regional climatic influences on surface temperature and precipitation in the South Shetland Islands, northern Antarctic Peninsula. An. Acad. Bras. Cienc. 95, e20230685 https://doi.org/10.1590/0001-3765202320230685.

Turner, J., Lachlan-Cope, T., Colwell, S., Marshall, G.J., 2005. A positive trend in western Antarctic Peninsula precipitation over the last 50 years reflecting regional and Antarctic-wide atmospheric circulation changes. Ann. Glaciol. 41, 85–91. https://doi.org/10.3189/172756405781813177.

Turner, J., Lu, H., White, I., King, J.C., Phillips, T., Hosking, J.S., Deb, P., 2016. Absence of 21st century warming on Antarctic Peninsula consistent with natural variability. Nature 535 (7612), 411–415. https://doi.org/10.1038/nature18645.

Turner, J., Marshall, G.J., Clem, K., Colwell, S., Phillips, T., Lu, H., 2020. Antarctic temperature variability and change from station data. Int. J. Climatol. 40 (6), 2986–3007. https://doi.org/10.1002/joc.6378.

Van Meijgaard, E., Van Ulft, L.H., Van de Berg, W.J., Bosveld, F.C., Van den Hurk, B.J.J. M., Lenderink, G., Siebesma, A.P., 2008. The KNMI Regional Atmospheric Climate Model RACMO, Version 2.1. KNMI, De Bilt, The Netherlands, p. 43.

Van Wessem, J.M., Ligtenberg, S.R.M., Reijmer, C.H., van de Berg, W.J., van den Broeke, M.R., Barrand, N.E., Thomas, E.R., Turner, J., Wuite, J., Scambos, T.A., van Meijgaard, E., 2016. The modelled surface mass balance of the Antarctic Peninsula at 5.5 km horizontal resolution. Cryosphere 10, 271–285. https://doi.org/10.5194/tc-10-271-2016.

Van Wessem, J.M., Van De Berg, W.J., Noël, B.P., Van Meijgaard, E., Amory, C., Birnbaum, G., Van Den Broeke, M.R., 2018. Modelling the climate and surface mass balance of polar ice sheets using RACMO2–part 2: Antarctica (1979–2016). Cryosphere 12 (4), 1479–1498. https://doi.org/10.5194/tc-12-1479-2018.

Vaughan, D.G., 2006. Recent trends in melting conditions on the Antarctic Peninsula and their implications for ice-sheet mass balance and sea level. Arct. Antarct. Alp. Res. 38 (1), 147–152. https://www.jstor.org/stable/4095837.

Vignon, É., Roussel, M.-L., Gorodetskaya, I., Genthon, C., Berne, A., 2021. Present and future of rainfall in Antarctica. Geophys. Res. Lett. 48 https://doi.org/10.1029/2020GL092281 e2020GL092281.

Wallis, B.J., Hogg, A.E., van Wessem, J.M., Davison, B.J., van den Broeke, M.R., 2023. Widespread seasonal speed-up of West Antarctic Peninsula glaciers from 2014 to 2021. Nat. Geosci. 16 (3), 231–237. https://doi.org/10.1038/s41561-023-01131-4.

Wang, S., Liu, G., Ding, M., Chen, W., Zhang, W., Lv, J., 2021. Potential mechanisms governing the variation in rain/snow frequency over the northern Antarctic Peninsula during austral summer. Atmos. Res. 263, 105811 https://doi.org/10.1016/j.atmosres.2021.105811.

Weidemann, S.S., Sauter, T., Malz, P., Jaña, R., Arigony-Neto, J., Casassa, G., Schneider, C., 2018. Glacier mass changes of lake-terminating grey and Tyndall glaciers at the southern Patagonia icefield derived from geodetic observations and energy and mass balance modeling. Front. Earth Sci. 6, 81. https://doi.org/10.3389/feart.2018.00081.

Wille, J.D., Favier, V., Dufour, A., Gorodetskaya, I.V., Turner, J., Agosta, C., Codron, F., 2019. West Antarctic surface melt triggered by atmospheric rivers. Nat. Geosci. 12 (11), 911–916. https://doi.org/10.1038/s41561-019-0460-1.

Wille, J.D., Favier, V., Gorodetskaya, I.V., Agosta, C., Kittel, C., Beeman, J.C., Codron, F., 2021. Antarctic atmospheric river climatology and precipitation impacts. J. Geophys. Res. Atmos. 126 (8) https://doi.org/10.1029/2020JD033788 e2020JD033788.

Wille, J.D., Favier, V., Jourdain, N.C., Kittel, C., Turton, J.V., Agosta, C., Berchet, A., 2022. Intense atmospheric rivers can weaken ice shelf stability at the Antarctic Peninsula. Commun. Earth Environ. 3 (1), 90. https://doi.org/10.1038/s43247-022-00422-9.

Zekollari, H., Huss, M., Farinotti, D., 2020. On the imbalance and response time of glaciers in the European Alps. Geophys. Res. Lett. 47 (2) https://doi.org/10.1029/2019GL085578 e2019GL085578.

Zhang, B., Yao, Y., Liu, L., Yang, Y., 2021. Interannual ice mass variations over the Antarctic ice sheet from 2003 to 2017 were linked to El Niño-Southern Oscillation. Earth Planet. Sci. Lett. 560, 116796 https://doi.org/10.1016/j.epsl.2021.116796.

Zou, X., Rowe, P.M., Gorodetskaya, I., Bromwich, D.H., Lazzara, M.A., Cordero, R.R., Bai, L.S., 2022. Strong warming over the Antarctic Peninsula during combined atmospheric river and Foehn events: contribution of shortwave radiation and turbulence. J. Geophys. Res. Atmos. https://doi.org/10.1029/2022JD038138 e2022JD038138.